Atmospheric Research 300 (2024) 107262

Contents lists available at ScienceDirect

Atmospheric Research

journal homepage: www.elsevier.com/locate/atmosres

Simulations of a tornadic supercell event in the south of Spain: Sensitivity to initial and boundary conditions and microphysics parameterizations

Francisco Javier Bello-Millán [a,c,*], Julián Palacios [b], Paloma Gutierrez-Castillo [c], Luis Parras [c]

[a] AEMET (State Meteorological Agency), Malaga, Spain
[b] AEMET (State Meteorological Agency), Madrid, Spain
[c] Universidad de Malaga, Escuela de Ingenierias Industriales, Malaga, Spain

ARTICLE INFO

2000 MSC:
0000
1111
PACS:
0000
1111
Keywords:
Severe convection
Supercell
Tornado
Spain
WRF
Microphysics

ABSTRACT

A tornadic supercell near the village of Campillos (Malaga province) occurred on 26 August 2019 with several associated damages. In this study, we analyze the sensitivity of the Weather Research and Forecasting (WRF) model to initial and boundary conditions and microphysics parameterizations when reproducing this particular event. A total of 20 cases were simulated with four initial and boundary conditions (ERA5, GDAS/FNL, GFS, HRES-IFS) and five microphysics parameterizations (WDM6, Goddard, Morrison, Thompson, WSM6). Forecasts are quantitatively compared with 10-min observations at 153 weather stations for the following variables: temperature at 2 m (T_2), relative humidity at 2 m (RH_2), wind speed at 10 m (U_{10}) and accumulated precipitation in 3 h (PCP_{3h}). Similarly, the spatial verification method MODE (Method for Object-Based Diagnostic Evaluation) has been used to evaluate the reproduction of convective storms by high-resolution numerical simulations. Our results indicate that microphysics plays a key role in this event, being more relevant than initial and boundary conditions. In particular, Goddard configuration combined with ERA5 or IFS initial and boundary conditions has shown the best overall performance. Simulation based on Goddard and ERA5 captured features to diagnose the development of severe convection. Therefore, WRF model, with the correct parameter sets, was able to reproduce the environmental conditions for supercell formation. The spatial resolution used in the simulations was appropriate to explicitly generate a supercellular storm, although it was not sufficiently high to resolve the formation of tornadoes. Nevertheless, the model showed signs of an environment favourable to tornadogenesis.

1. Introduction

Meteorological numerical simulations are essential for predicting hazardous phenomena and mitigating their consequences. Supercell storms are a violent type of convective storms that can lead to tornadic events. Due to the dramatic consequences of the most extreme episodes, supercell events have been analyzed for a long time, but their very complex dynamics (Klemp and Rotunno, 1983) make the analysis challenging. Additionally, the strongly nonlinear physical processes intrinsic to tornadoes make the correct prediction of a tornado-spawning supercell path and intensity a complex process.

Supercell events are not uncommon in Spain and their study and interest have increased in recent years, extending the knowledge about these systems in the country. Martín et al. (Martín et al., 2021) identified >100 supercells per year on average in Spain in the period of 2014 to 2019. Even though most of these events have a low impact on society, some of them have dramatic consequences since supercells might produce severe weather phenomena such as flash floods, severe wind gusts, hail and tornadoes. Although there is no specific data collected on the damage created only by supercells, according to the national insurance agency "Consorcio de Compensación de Seguros", in the period 1987–2021 the category which includes damages produced by *extraordinary winds, tornadoes and flooding due to precipitation* represents 16.0% of all payments (45.7% of the total claims) (Consorcio de Compensación de Seguros, 2021).

There are more tornadoes and supercells in NE Spain and therefore more bibliography referring to severe events in this region with increasing productivity since the beginning of the century (Gayà et al., 2001; Bech et al., 2007; Aran et al., 2009; Romero et al., 2015; Rodríguez and Bech, 2018; Bech et al., 2015). However, there are still relevant events in the SW region, which is the region where our study is located. In fact, the major tornado event registered in Spain occurred in Cadiz in

* Corresponding author at: AEMET (State Meteorological Agency), Demostenes 4, 29010 Malaga, Spain.
E-mail address: fbellom@aemet.es (F.J. Bello-Millán).

https://doi.org/10.1016/j.atmosres.2024.107262
Received 30 March 2023; Received in revised form 27 December 2023; Accepted 17 January 2024
Available online 24 January 2024

1671 (Sánchez-Laulhé, 2005). The characteristics of the SW region events include some important physical differences with respect to the NE episodes. The most relevant difference is associated with the seasonality of the event. Southwestern events mainly occur in the cool season when surface specific humidity is lower than in the warm season (Rodríguez and Bech, 2021; Riemann-Campe et al., 2009). The study presented by Gayà in 2011 (Gayà, 2011) is an excellent source for a first approach to the main characteristics of tornadoes and severe storms in Spain. In that study, Gayà shows an interesting approach analyzing different time periods up to 2009, focusing on the geographical and temporal variations as a function of societal changes.

In general, obtaining information about some meteorologically relevant events is challenging, especially if they are developed in rural areas. Nowadays, with the use of fast communication and the facility of capturing images, the relevance of including information gathered from the general public is key to complete scientific databases. Martín et al. (Martín et al., 2021) were able to combine volunteers and public effort to develop a database on supercell events. They gathered information about 703 thunderstorms with supercell characteristics in a six-year study period (January 2014 to December 2019). Some other studies collected a relevant number of events, such as Rodríguez and Bech (Rodríguez and Bech, 2021), Calvo et al. (Calvo-Sancho et al., 2022) or Quirantes et al. (Quirantes Calvo et al., 2022). Rodríguez and Bech (Rodríguez and Bech, 2021) presented a compilation with around 900 tornado and waterspout events recorded from 1980 to 2018 in convective environments in the Iberian Peninsula and Balearic Islands (western Mediterranean). They showed that tornadoes in the southwestern Iberian Peninsula are associated with higher-shear, lower-CAPE environments than in the northeast. Even more recently Calvo et al. (Calvo-Sancho et al., 2022) analyzed a dataset of 262 supercells during

Fig. 1. Study area. Top: Global map containing the southwestern part of Europe and northwestern part of Africa with a rectangle locating Andalusia region. Bottom left: Map containing the main cities, rivers and mountain systems of Andalusia (note that Guadalhorce River is labeled on its mouth). Bottom right: Zoom into the interest region. The approximate trajectory of the supercell from 17:10 to 19:10 UTC is depicted in red line with black dots. Dots are evenly spaced in time by 10 min intervals. Also, centroids of the estimated affected zone by the tornadoes are represented by T1, T2 and T3. Source: (Jiménez Alonso et al., 2020). (For interpretation of the references to colour in this figure legend, the reader is referred to the web version of this article.)

2011–2020 and Quirantes et al. (Quirantes Calvo et al., 2022) collected 565 cases in the period 2017–2021 and used a subset of 497 cases to characterize the environmental conditions in the formation of supercells. Their results highlight that, in Spain, supercells typically form in environments with lower CAPE and storm relative helicity than those in USA.

Our study focuses on an episode developed on 26 August 2019 in the southern region of Spain, Andalusia. Fig. 1 shows a map of Andalusia with its orography and main cities and provinces to help the reader. The small region where the event happened is marked in a brown box. This specific region near the border between the Malaga and Seville provinces reported historically hazardous weather conditions such as the terrible flood in La Roda de Andalucía and Casariche in 1973, the torrential rains in Campillos in 1969 or the recent event in Antequera in 2018.

This work aims to evaluate the predictability of this severe weather event and provide insight into the suitable configurations or strategies for modelling this kind of episode. The studied case was numerically simulated by using the WRF model (Skamarock et al., 2021) with a horizontal resolution of 1 km to reproduce the mesoscale conditions of the study area. WRF has been widely used to reproduce organized deep moist convection episodes at kilometric scale (see, *e.g.*, (Taszarek et al., 2016; Pilguj et al., 2019; Avolio and Miglietta, 2021; Spiridonov et al., 2021; Toker et al., 2021)). This model contains several parameterization options for physical processes such as the planetary boundary layer (PBL), microphysics, cumulus or radiation. Each of these options and their combinations affect the outcome of the simulations. Therefore, a sensitivity analysis of the different parameters is crucial to enhance the outcome. In this paper, we performed a sensitivity analysis with 20 simulations involving five distinct microphysics schemes and four distinct initial and boundary conditions (hereafter IBC). Apart from cumulus convection schemes (not considered in our high-resolution simulations since they are convection-permitting), microphysics parameterizations are the leading physics schemes in rainfall forecasting (Liu et al., 2020). These parameterizations influence the convection initiation in mesoscale simulations (Schwitalla et al., 2020). Moreover, the sensitivity associated with global models has been explored to consider the possibility of substantial effects on mesoscale simulations (Kumar et al., 2017).

Both a point-based and a spatial verification analysis were performed to distinguish the best pairs of IBC and microphysics to reproduce the event. This combined verification approach allows us to cope with the double penalty issue, which arises when evaluating high-resolution models by means of traditional methods (Cassola et al., 2015). In addition, spatial verification methods are closer to human evaluation than point-based methods (Tapiador et al., 2019).

This paper is organized as follows. Section 2 contains the case description. Section 3 describes the methodology used in this analysis, including: (1) details of the performed numerical simulations; (2) the use of the observations and (3) details about validation and verification methods. Section 4 summarizes the verification results of the paper compared against observations. Section 5 describes the mesoscale environment and convective features reproduced with the best performing setting. Section 6 is devoted to the conclusions of this work.

2. Case description

This work focuses on the formation of a supercell and three tornadoes on 26 August 2019 in the southern region of Spain (Andalusia), in the province of Malaga. Specifically, the tornadoes were found in the area around the village of Campillos, which is located near the limit of the province of Seville (see Fig. 1). This specific region is surrounded by two mountain chains creating a singular orography that plays a crucial role in the studied case, as will be described in Section 2.1. The episode was extensively studied and documented by AEMET (Spanish State Meteorological Agency) meteorologists and their findings and reports were published in a technical note in 2020 (Jiménez Alonso et al., 2020). Some of the main characteristics of the episode are repeated here for clarity. In the following subsections, we summarize the main aspects of the synoptic conditions, meteorological observations and impacts associated with this multiple tornadic event.

2.1. Synoptic and mesoscale environment

During the preceding days, an upper level trough moved over the Atlantic Ocean and evolved into a cut-off low as it approached the Iberian Peninsula. On 26 August, it encompassed large areas of Spain and Portugal and exerted an intense dynamic forcing in the study area, owing to vorticity advection and to a southwesterly jet exceeding 75 knots at 300 hPa (Fig. 2). This synoptic circulation pattern has been related to the development of tornadoes in the Iberian Peninsula (Rodríguez and Lemus-Canovas, 2023), and to intense precipitation events in the Spanish Mediterranean area (Riesco et al., 2014).

Fig. 3a shows the middle and upper level diagnosis corresponding to the same valid time as in Fig. 2. The map highlights a cold anomaly of −13 °C and two vorticity centers within the low core. The upper-level jet crosses Spain from the southwest to the northeast, entering over the Gulf of Cadiz. Additionally, Fig. 3b depicts the surface diagnosis. The Peninsula is influenced by a broad area of low pressure concentrated in northern Africa, while high pressures predominate in the Atlantic Ocean and eastern and central Europe. This setup favors the low-level easterly winds over Andalusia, which constitute a supply of moisture from the Mediterranean Sea through the Guadalhorce Valley. Furthermore, the combination of southwesterly and easterly winds approaching the Strait of Gibraltar produces a convergence zone to the northwest of the province of Malaga (Fig. 4). This low-level flow configuration is similar to other severe weather episodes in the south of the Iberian Peninsula (Sánchez-Laulhé et al., 2014).

In their study, Jiménez et al. (Jiménez Alonso et al., 2020) applied the conceptual model of water vapor plume introduced by Thiao et al. (Thiao et al., 1993) to explain the situation. Indeed, a well-defined band of moisture can be distinguished in the METEOSAT 6.2 channel (Fig. 5a), whose axis goes from Canary Islands to the south of France, where the flow is diffluent. The plume (marked with green arrows over the Iberian Peninsula in Fig. 5a and b) is located to the west of an upper-level ridge (Fig. 3a) and in the inlet of moist unstable air from subtropical latitudes. The moisture gradient is intense across the plume, both in upper (Fig. 5a) and middle levels (Fig. 5b) of the troposphere. The air is much drier to the west, in the cut-off low region, than to the east of the plume. This distinction between air masses is also pronounced at low levels (Fig. 5c). The equivalent potential temperature field (θ_e) shows the interaction of a cold and dry polar air mass and a warm and moist tropical one. A low-level θ_e-ridge curves northwestward from northern Africa and crosses the plume in the interior of the Iberian Peninsula with a region of strong θ_e-gradient separating both air masses (the θ_e-ridge axis is marked with a dashed red line in Fig. 5c).

2.2. Observations

There are plenty of observations on the event near the studied area. The closest automatic weather stations have rain gauges, anemometers and vanes, among other instruments, allowing the analysis of the local wind and the total precipitation during the entire episode. Furthermore, reflectivity and doppler velocity measured by different radars are also available for analysis, which is useful for dynamically following the evolution of the convective systems of interest.

In Fig. 6, we present a sequence of radar reflectivity PPI images (Plan Position Indicator) showing highlights of the most intense convection, which happened from 15:30 to 20:00 UTC (a detailed description of the event is available in Jiménez et al. (Jiménez Alonso et al., 2020)). The first storms developed before 15:30 UTC close to the town of Osuna, in Seville (Fig. 6 (a)). The flow in the surrounding area favored both the

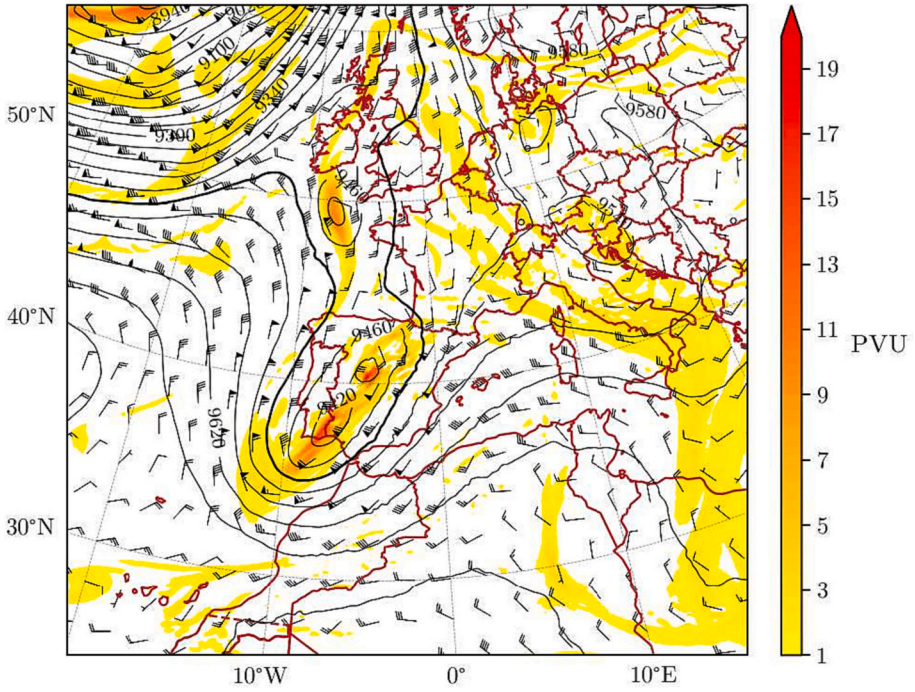

Fig. 2. Potential vorticity in PVU (shaded), geopotential height in gpm (black contours) and wind barbs at 300 hPa for HRES-IFS operational analysis. Base time: 26 August 2019 at 12:00 UTC (14:00 LT).

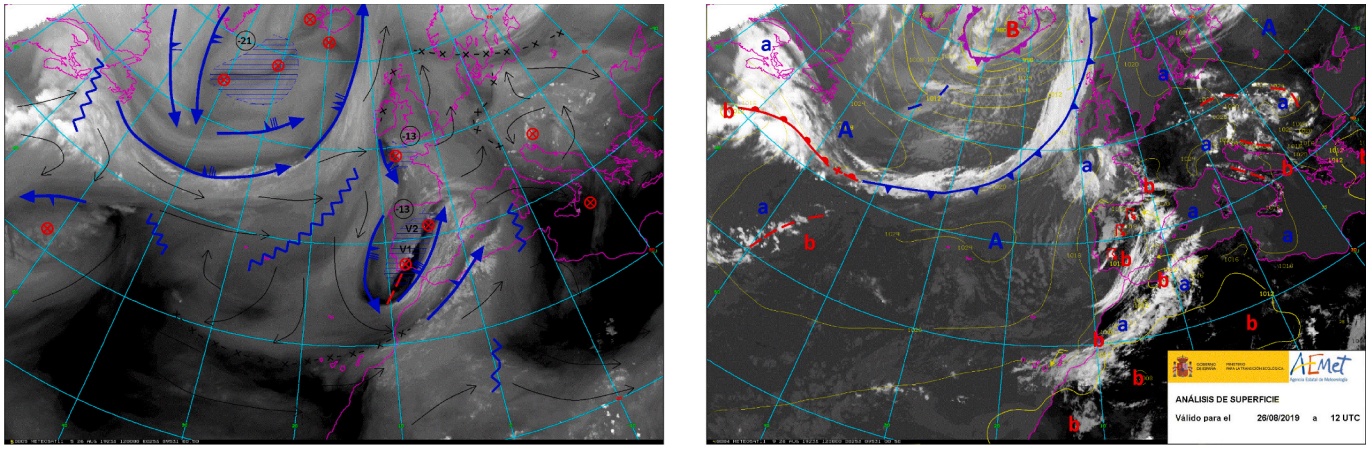

Fig. 3. Middle and upper levels (a) and surface (b) diagnosis of 26 August at 12:00 UTC (14:00 LT). In the maps, "B" and "b" stand for low pressure; "A" and "a" refer to high pressure. Both diagnosis are superimposed on satellite images: METEOSAT water vapor 6.2 for middle and upper level and METEOSAT infrared 10.8 in the case of surface diagnosis. Source: AEMET.

organization and the northeastern displacement of the storms. One of the storms intensified and deepened by 17:00 UTC, in the province border of Sevilla and Malaga, and split at around 17:16 UTC forming a right moving (R_1) and a left moving storm (L_1), as depicted in Fig. 6 (b). From the moment the split occurred, R_1 increased its intensity and moved slowly around northern Malaga, and by 17:50 UTC showed characteristics of a low precipitation (LP) supercell, while L_1 traveled northwards and presented lower reflectivity, as can be seen in Fig. 6 (c). This lower intensity of L_1 could be explained, at least in part, due to the fact that R_1 stayed in between L_1 and the radar, and so the radar beam suffered an attenuation when interacting with R_1.

The storm R_1 weakened from 17:50 until 18:10 UTC, staying mostly stationary around the province limit of Seville and Malaga. This weakening could be explained by the disruption of the southwesterly incoming flow which fed the updraft due to the precipitation downdraft and the presence of the mountain range Sierra de los Caballos (see zoom in Fig. 1). Although orography could have been responsible for the dissipation of the storm, it probably supported the activation of the mesocyclone in R_1. The humid southeasterly flow coming from the Alboran Sea, mentioned in Subsection 2.1 (see Fig. 4), moved up to Sierra de los Caballos and was ingested into the storm in middle levels. The wind speed and direction time series recorded by the Fuente de Piedra automatic weather station (Fig. 7) show a southern flow throughout all day until 19:00 UTC. At 18:10 UTC (Fig. 6 (d)), R_1 changed its bearing and started traveling southwards.

In the time lapse between and 18:10 and 19:00 UTC, R_1 seems to have evolved from a LP to high precipitation (HP) supercell (Fig. 6 (e)). Fig. 8 shows a detailed image of the reflectivity of R_1 for the 18:56 UTC

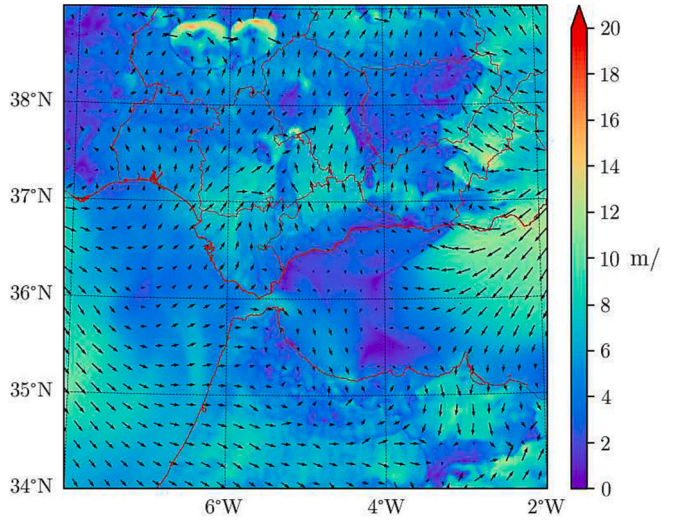

Fig. 4. Wind speed and direction at 10 m above the surface for HARMONIE-AROME operational analysis. Base time: 26 August at 15:00 UTC (17:00 LT).

radar sweep along with a doppler velocity image. There are several characteristic reflectivity signs in Fig. 8 (a) to determine that the storm was a right moving supercell. Additionally, the combination of incoming (green) and outgoing (orange) radial velocities shown in Fig. 8 (b) imply the presence of a mesocyclone. At 19:16 UTC, the signs of the presence of a mesocyclone disappeared, and the remaining multicellular system deviated from the preceding bearing and started a movement towards the west (Fig. 6 (f)). Finally, the convection fully dissipated at 20:00 UTC, when the humid flow from the Alboran Sea had already stopped.

Although the maximum wind gust recorded at Fuente de Piedra automatic station barely exceeded 50 km/h (Fig. 7), the maximum wind speed associated with the event probably reached higher values, according to the material damage recorded in the area. The rain gauge accumulations in 6 h, from 15:00 to 21:00 UTC, are represented in Fig. 9 (a). There was a considerable amount of precipitation accumulated around the border of the provinces of Malaga and Seville. Fig. 9b shows the accumulated precipitation estimated by the radar, at the same temporal period to illustrate the spatial distribution of the precipitation.

2.3. Impacts and damages

There are multiple pieces of evidence of at least three tornadoes around the villages of Sierra de Yeguas and Campillos which could be associated with the supercell R1 described in Subsection 2.2. The approximate temporal lifespans of the tornadoes are the following: Tornado 1 lasts from 18:00 to 18:35 UTC (20:00 to 20:35 LT), Tornado 2 from 18:45 to 19:15 UTC, and Tornado 3 started around 19:00 UTC, although there is a lack of precision on the starting time and its lifespan.

Tornado 1 impacted an area between Martín de la Jara and Sierra de Yeguas, about 5.5 km north of Campillos. Multiple images show that this tornado progressed very near to a double line of aerogenerators (Jiménez Alonso et al., 2020). Tornado 2 was located in the proximity of Campillos, in an agricultural and livestock area about 1.6 km northwest of the village. See Fig. 10 (a) in which the formation of the tornado in the proximity of the village is clear. This tornado traveled at least 700 m. The estimated trajectory of Tornado 2, followed from south to north, is displayed with an orange line in Fig. 10 (b). Some of these damages were: at least 6 industrial units destroyed, the death of >60 goats, broken power lines, and deteriorated regional roads. Furthermore, on-site observations show numerous trees damaged or even wholly uprooted and flying objects. By analyzing the tornado damages, it is possible to estimate that the tornado could be category EF1 (between 135 and 175 km/h of maximum speed) and momentaneously could rise

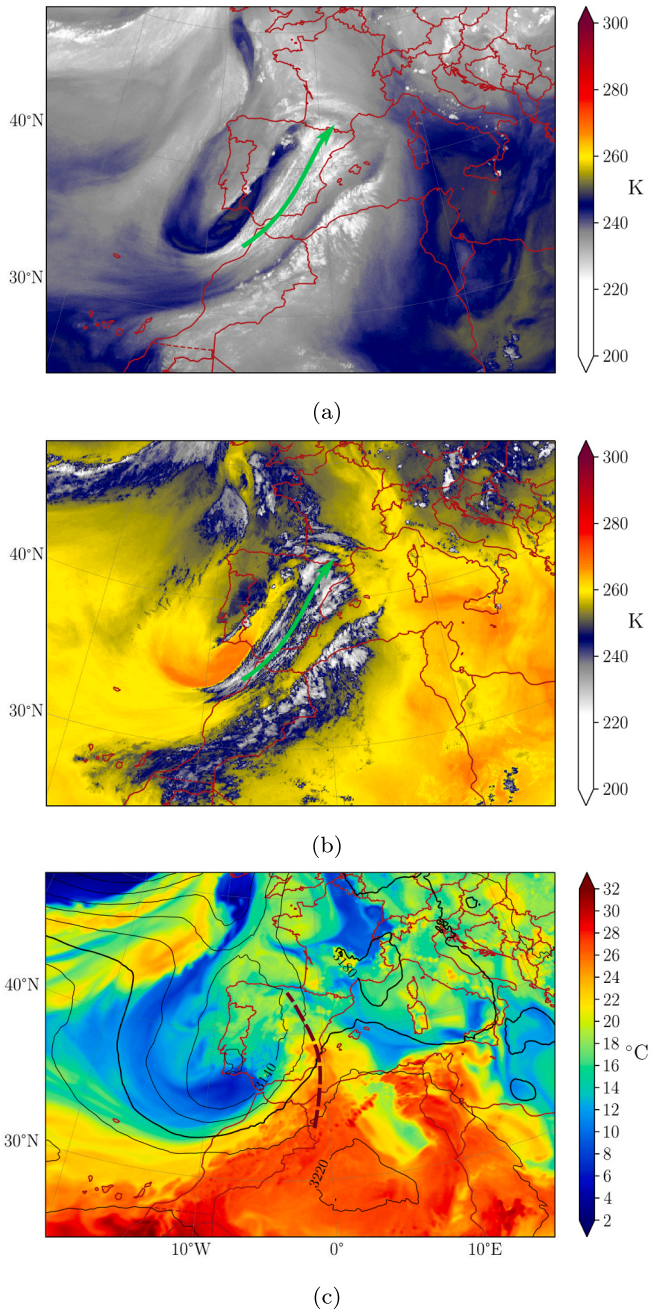

Fig. 5. Air masses analysis: (a) METEOSAT 6.2 channel brightness temperature in K; (b) METEOSAT 7.3 channel brightness temperature in K; (c) equivalent temperature at 700 hPa in °C (shaded) and geopotential height in gpm (black contours) for HRES-IFS operational analysis. Base time: 26 August at 12:00 UTC (14:00 LT).

to category EF2. Fig. 11 shows some of the tornado damages, such as a metallic entrance door, trees and fences, or construction materials and tools.

Tornado 3 was detected at about 19:00 UTC (21:00 LT) at the final stage of the supercell and located to the west of Campillos. There is a lack of precision about its temporal distribution and situation since it occurred at sunset, and there was no reported damage. However, its presence is confirmed by several graphical materials (Jiménez Alonso et al., 2020).

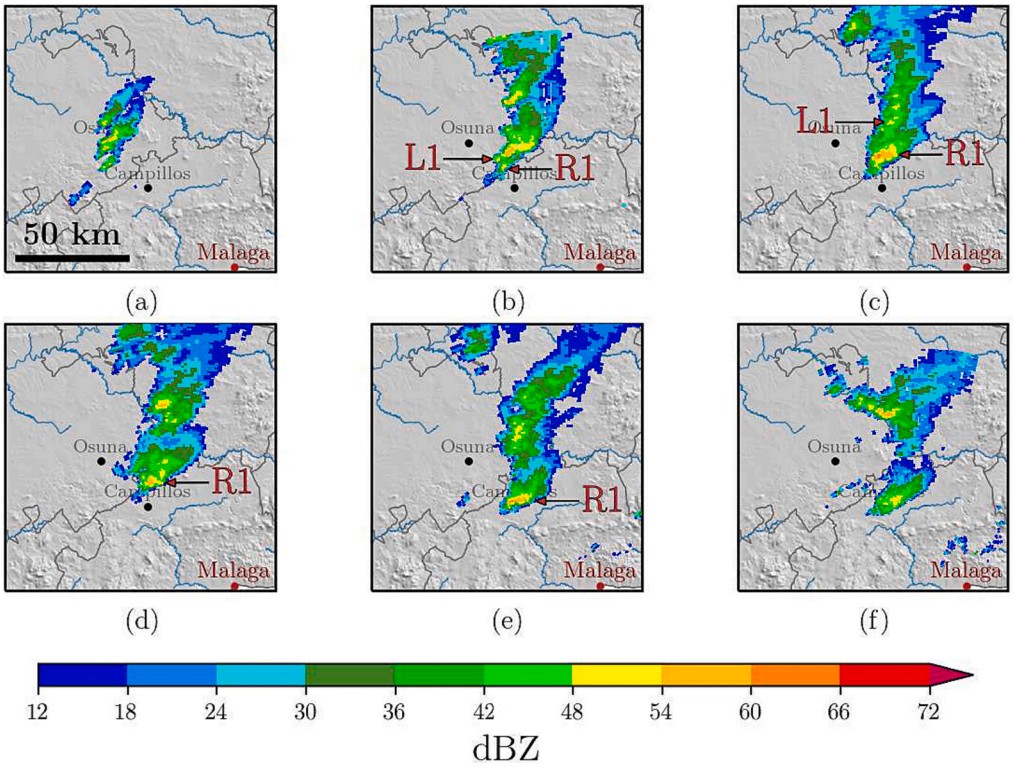

Fig. 6. Sequence of reflectivity images corresponding to the 0.5° elevation PPI from the radar of Malaga at the following UTC times: (a) 15:30; (b) 17:16; (c) 17:50; (d) 18:10; (e) 19:00; (f) 19:16.

3. Methodology

This section describes the mesoscale simulations performed to analyze the convective environment where the supercell developed. Observational data sources and verification methods are also detailed.

3.1. Numerical simulations

In this work, WRF-ARW model version 4.3 (Skamarock et al., 2021) was chosen to numerically reproduce the mesoscale conditions of 26 August 2019. WRF has been widely used to reproduce organized deep moist convection episodes at kilometric scale (see, *e.g.*, (Taszarek et al., 2016; Pilguj et al., 2019; Avolio and Miglietta, 2021; Spiridonov et al., 2021; Toker et al., 2021)). Therefore, the model setup consisted of three two-way nested domains of increasing resolution focusing on the area of interest: 9, 3, and 1 km (Fig. 12). The spatial and temporal resolution for each domain was of 250 × 250 horizontal grid cells and 45 s for d01, 451 × 451 and 15 s for d02, and 601 × 601 and 3 s for d03. Every simulation ran with 72 vertical levels ranging from the surface up to 40 hPa. Approximately 20 of these levels were below the first kilometer above the ground level. This arrangement was used in γSREPS, a LAM-EPS (Limited Area Model - Ensemble Prediction System) developed by AEMET (Callado Pallarés et al., 2019). The full form of SREPS is Short Range Ensemble Prediction System.

Domains d02 and d03 utilized Shuttle Radar Topography Mission (SRTM) topographic data, with around 90 m resolution (Farr et al., 2007). The simulations covered a period of 24 h, from 26 August 00:00 UTC to 27 August 00:00 UTC, and the first 12 h were discarded as spinup (we recall the reader that the most convective period encompassed from 15:30 to 20:00 UTC). Results from the innermost domain were stored with a temporal resolution of 10 min and compared against observational data for verification.

A total of 20 simulations were analyzed to conduct a sensitivity analysis. All of them performed with the Yonsei University scheme (YSU, (Hong et al., 2006)) for planetary boundary layer, the Rapid Radiative Transfer Model for GCMs (RRTMG, (Iacono et al., 2008)) for shortwave and longwave radiation, the Unified Noah Land Surface Model (Tewari et al., 2004) and the Tiedtke (Tiedtke, 1989) scheme for cumulus parameterization in the outermost domain. The analysis was performed considering four different IBC and five microphysics schemes. Simulations were nested to ECMWF ERA5 (Hersbach et al., 2020), ECMWF HRES-IFS (ECMWF, 2019), NCEP GFS (National Centers for Environmental Prediction et al., 2015a) and NCEP GDAS/FNL (National Centers for Environmental Prediction et al., 2015b). Thus, two operational forecasts (namely, HRES-IFS and GFS), one reanalysis (ERA5) and an operational analysis (GDAS/FNL) were considered. Characteristics of these global model/reanalysis datasets are included in Table 1. It must be noted that, since HRES-IFS horizontal resolution is approximately 9 km, mesoscale simulations based on this global model only had two domains (d02 and d03) and no cumulus parameterizations at all.

Regarding microphysics parameterization, the selected schemes in the sensitivity analysis were the following: Goddard (Tao et al., 1989; Tao et al., 2003), Morrison (Morrison et al., 2009), Thompson (Thompson et al., 2008), WRF Double Moment 6 class (WDM6, (Lim and Hong, 2010)) and WRF Single Moment 6 class (WSM6 (Hong and Lim, 2006)). Table 2 summarizes their main characteristics. All schemes consider six hydrometeor species (water vapor, cloud water, rain, ice, snow and graupel, but no hail) and differ in their complexity. Morrison, which is the most complex scheme, is double moment for rain, ice, snow and graupel. Similarly, WDM6 is double moment for cloud water and rain, and includes a prognostic variable of cloud condensation nuclei (CCN). Thompson is double moment for rain and cloud ice. Finally, Goddard and WSM6 are single moment for all species. According to WRF User's Guide, all these microphysics schemes are suitable for high resolution simulations. For the sake of simplicity, abbreviated names are given to each test by virtue of its IBC and microphysics scheme (Table 3).

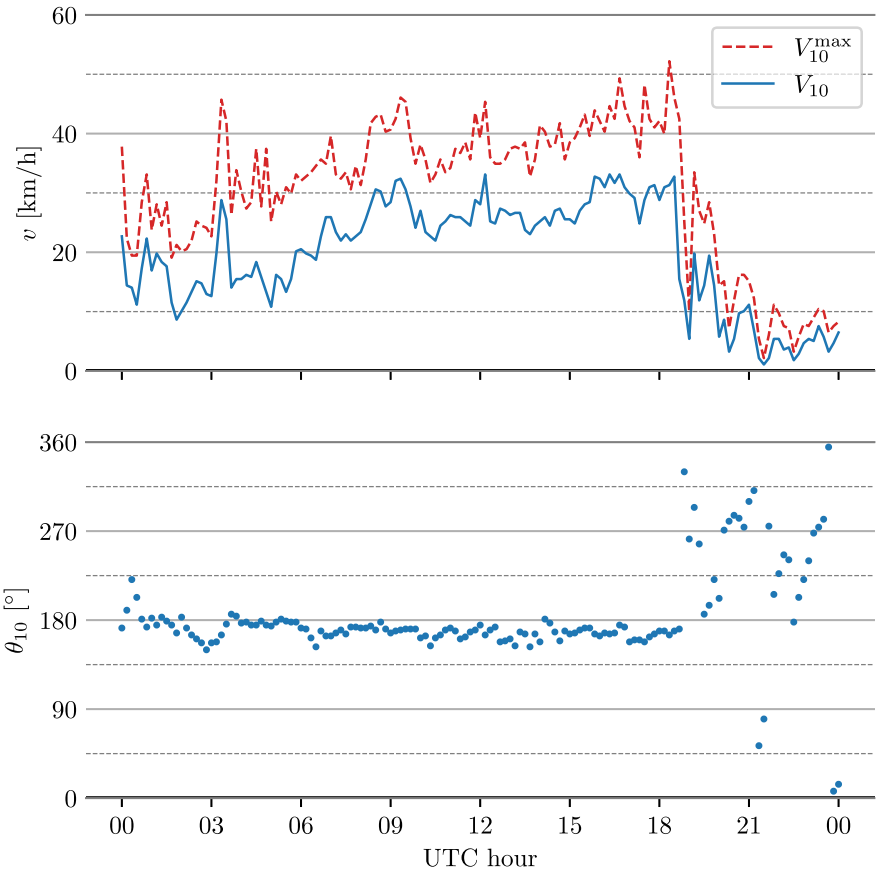

Fig. 7. Fuente de Piedra weather station data corresponding to 26 August: Maximum wind gust in 10 min, V_{10}^{max} and wind speed at 10 m, V_{10} (top); wind direction at 10 m, θ_{10} (bottom).

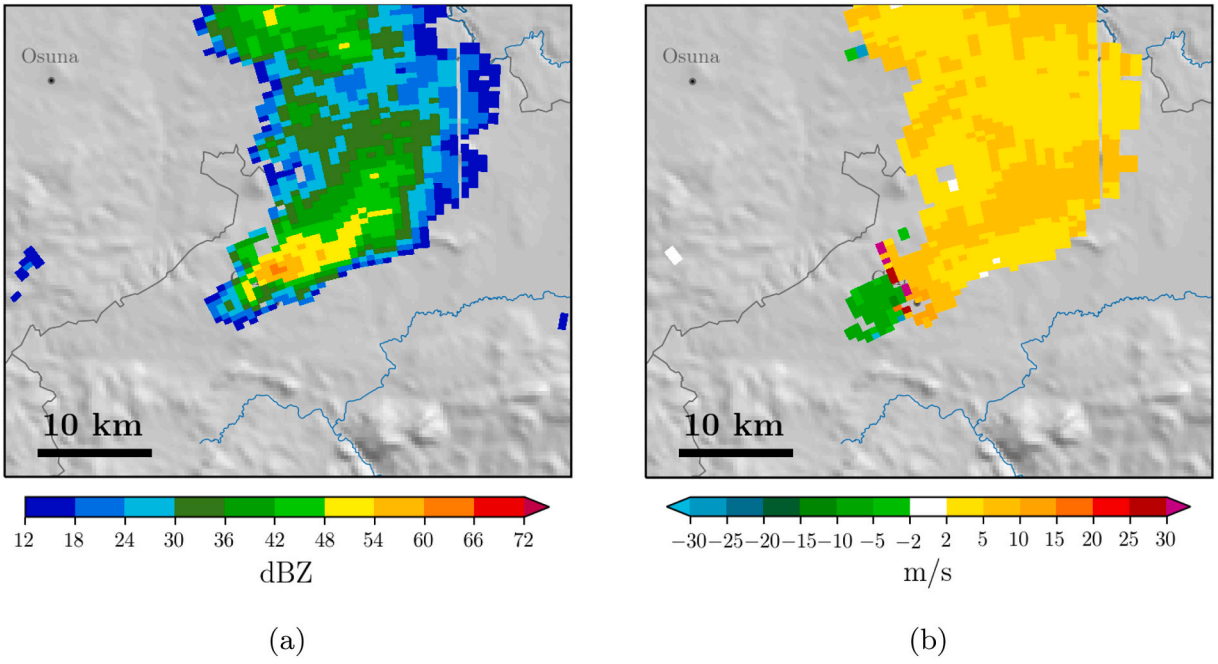

Fig. 8. Detail of storm R_1 at 18:56 UTC: (a) radar reflectivity; (b) doppler velocity. The height of the radar beam over Campillos is 1300 m, approximately.

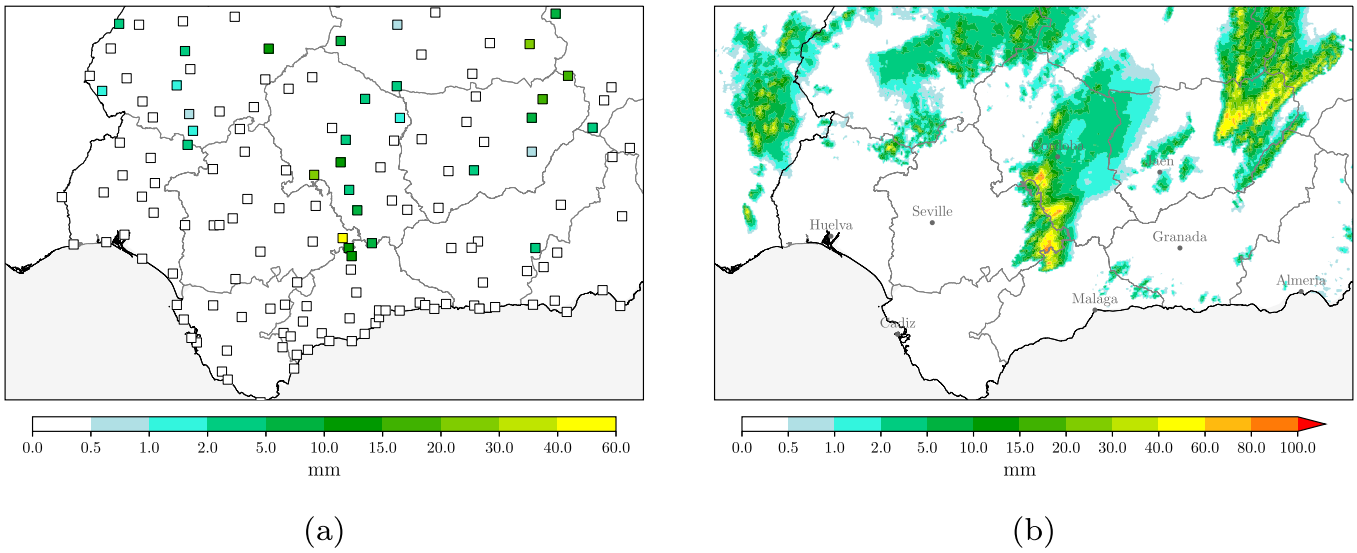

Fig. 9. Left: Accumulated precipitation between 15:00 and 21:00 UTC on 26 August registered by the rain gauges available in the automatic weather stations. Right: Estimated accumulated precipitation from radar data for the same period.

Fig. 10. (a) Picture of the Tornado; (b) estimated trajectory of Tornado 2 from south to north (Jiménez Alonso et al., 2020). Map rendered with Google Earth.

Fig. 11. Damages created by Tornado 2 (Jiménez Alonso et al., 2020). From left to right: metallic entrance door, damaged trees and fences, and construction materials and tools.

3.2. Observational data for verification purpose

In order to obtain a quantitative evaluation of the simulations, different verification methods were used depending on which meteorological variable was considered. First, we have conducted a point-based verification process based on temperature, relative humidity, wind speed and precipitation obtained from the automatic weather stations (AWS), see Section 3.3. Fig. 13 shows the spatial domain selected for the verification (d03) together with the data acquisition stations containing relevant information about the verification area. Second, we performed a spatial verification analysis based on the reflectivity of the images captured by three nearby radars, see Section 3.4. These radars are located in the provinces of Seville, Malaga and Murcia, respectively. Their specific locations are marked on Fig. 13.

3.3. Verification scores

Scores as BIAS, Root Mean Square Error (RMSE) and correlation coefficient (ρ) were chosen to evaluate the performance of the temperature at 2 m (T_2), relative humidity at 2 m (RH_2), 10-min mean wind

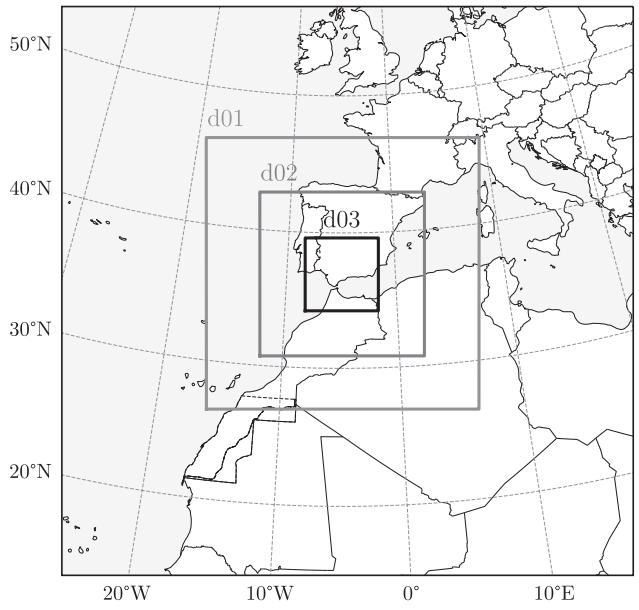

Fig. 12. WRF domains for mesoscale simulations.

Table 1
Characteristics of initial and boundary conditions datasets. This information corresponds to the archived data for the simulation date. Δt is the time interval between consecutive updates in boundary conditions.

Global model	Horizontal resolution	Vertical levels	Δt
ERA5	0.25°	137 hybrid sigma/pressure levels up to 0.01 hPa	1 h
HRES-IFS	0.1°	137 hybrid sigma/pressure levels up to 0.01 hPa	1 h
GFS	0.25°	34 pressure levels up to 1 hPa	3 h
GDAS/FNL	0.25°	34 pressure levels up to 1 hPa	6 h

Table 2
Summary of microphysics parameterizations and their prognostic variables. Q refers to the mixing ratio; while subscripts stand for hydrometeor species: cloud (c), rain (r), ice (i), snow (s) and graupel (g). N is the number of hydrometeors and N_n is the CCN number. Source: WRF User's Guide.

Microphysics scheme	Single/double moment	Mass variables	Number variables
WDM6	Double	Q_c, Q_r, Q_i, Q_s, Q_g	N_n, N_c, N_r
Goddard	Single	Q_c, Q_r, Q_i, Q_s, Q_g	
Morrison	Double	Q_c, Q_r, Q_i, Q_s, Q_g	N_r, N_i, N_s, N_g
Thompson	Double	Q_c, Q_r, Q_i, Q_s, Q_g	N_r, N_i
WSM6	Single	Q_c, Q_r, Q_i, Q_s, Q_g	

speed at 10 m (U_{10}) and accumulated precipitation in 3 h (PCP_{3h}). The observations corresponding to these variables were obtained for 10 min intervals from 153 weather stations belonging to different Spanish public organisms (see Fig. 13). Results from the numerical simulations were interpolated, using bilinear interpolation, to each location to establish forecast-observed pairs. In the following, we include brief definitions of these metrics. More complete descriptions can be found in (Wilks, 2019) or (Jolliffe and Stephenson, 2012).

BIAS is the averaged difference between forecasts and observations. It represents systematic errors, and its positive (negative) sign indicates a general overestimation (underestimation) of the studied variable. Given N pairs of data (number of stations multiplied by the number of time steps), BIAS is computed as:

Table 3
Summary of simulations and their abbreviations and symbols in graphs.

Initial and boundary conditions	Microphysics	Abbreviation	Symbol
ERA5	WDM6	ED	◊
	Goddard	EG	□
	Morrison	EM	Δ
	Thompson	ET	☆
	WSM6	EW	○
GDAS/FNL	WDM6	FD	◊
	Goddard	FG	□
	Morrison	FM	Δ
	Thompson	FT	☆
	WSM6	FW	○
GFS	WDM6	GD	◊
	Goddard	GG	□
	Morrison	GM	Δ
	Thompson	GT	☆
	WSM6	GW	○
HRES-IFS	WDM6	HD	◊
	Goddard	HG	□
	Morrison	HM	Δ
	Thompson	HT	☆
	WSM6	HW	○

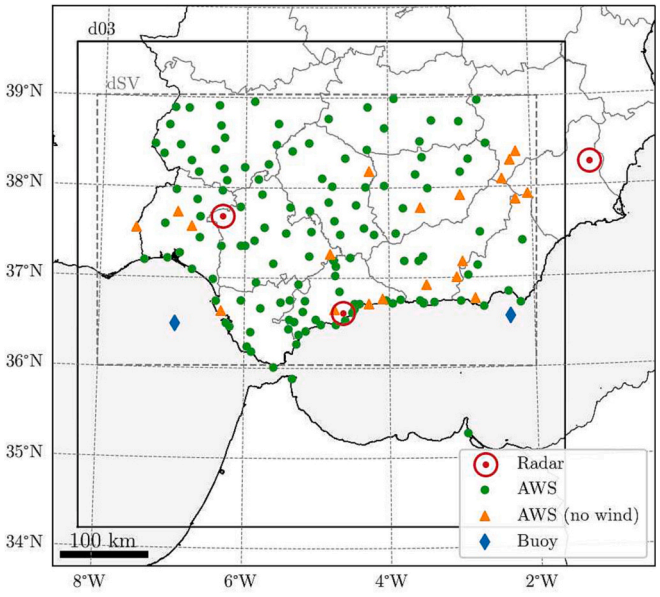

Fig. 13. Observational data. Automatic weather stations (AWS) with and without wind velocity measurements from AEMET network and two buoys property of Puertos del Estado. Spatial verification domain (area dSV) and radars of Sevilla (westernmost), Malaga (center) and Murcia (easternmost).

$$\mathrm{BIAS} = \frac{1}{N}\sum_{i=1}^{N}(F_i - O_i), \tag{1}$$

where F stands for forecast and O for observation, and i refers to the observations at the various meteorological stations used for the times for which there are recorded logs. Since BIAS is not an accuracy metric, its information can be complemented by using the Root Mean Square Error (RMSE) which considers the size of individual differences. The Root Mean Square Error (RMSE) is defined as the square root of the averaged squared error:

$$\mathrm{RMSE} = \sqrt{\frac{1}{N}\sum_{i=1}^{N}(F_i - O_i)^2}. \tag{2}$$

According to (Taylor, 2001; Delle Monache et al., 2011), RMSE can be decomposed as:

$$\mathrm{RMSE}^2 = \mathrm{CRMSE}^2 + \mathrm{BIAS}^2, \tag{3}$$

where CRMSE is the Centered Root Mean Square Error, the random component of RMSE. CRMSE provides an indication of the error other than BIAS, and it can be associated with the intrinsic predictive skill of the forecast. Its mathematical expression is the following:

$$\mathrm{CRMSE}^2 = \frac{1}{N}\sum_{i=1}^{N}\left[(F_i - \overline{F}) - (O_i - \overline{O})\right]^2 = \sigma_F^2 + \sigma_O^2 - 2\sigma_F\sigma_O\rho, \tag{4}$$

where $\overline{F}$ is the averaged forecast over the N values, $\overline{O}$ is the averaged observation, σ_F is the standard deviation of forecast, σ_O is the standard deviation of observations and ρ is the Pearson correlation coefficient between forecast and observations. ρ measures the linear dependence between two variables and is computed as:

$$\rho = \frac{\sum_{i=1}^{N}(F_i - \overline{F})(O_i - \overline{O})}{\sqrt{\sum_{i=1}^{N}(F_i - \overline{F})^2}\sqrt{\sum_{i=1}^{N}(O_i - \overline{O})^2}}. \tag{5}$$

This approach enables the generation of Taylor diagrams (after (Taylor, 2001)), which jointly incorporate ρ, CRMSE, σ_F and σ_O.

3.4. Spatial verification

Point-based verification may be misleading in assessing the forecast skill when dealing with high resolution simulations due to the double penalty issue (Davis et al., 2006; Karki et al., 2018). This effect arises when a simulation slightly misplaces a meteorological feature. In such case, traditional scores penalize twice the forecast considering both a non-detection (where it is observed but not forecast) and a false alarm (where it is forecast but not observed). The double penalty is more relevant for non-smooth variables such as precipitation.

In order to cope with this problem, different spatial verification methods have been developed during the last decades (see (Gilleland et al., 2009) for the sake of comparison). We selected the feature-based Method for Object-Based Diagnostic Evaluation (MODE, (Davis et al., 2006)), which is implemented in the NCAR MET verification tool. MODE has properly evaluated the reproduction of structures like convective systems by high-resolution simulations (Cassola et al., 2015).

This verification technique is based on object identification in both observation and forecast fields. The process consists of two steps: convolution and thresholding. First, raw fields are smoothed to filter isolated features and retain essential information. Subsequently, a threshold is applied to the convoluted field for object identification. Two parameters govern the identification, namely the convolution radius and the threshold. There is not a universally optimal setting for these parameters. The election depends on the application and the purpose of the verification. This study considered a convolution radius of 3 km and a threshold of 35 dBZ (this value is typically found in convective storms; see (Duda and Turner, 2021) for a sensitivity analysis of reflectivity thresholds).

After identifying objects, MODE retrieves geometric features such as area, centroid position, axis angle, curvature, aspect ratio, complexity or intensity. The similarity between a pair of forecast-observed objects is computed using a fuzzy logic algorithm to obtain the total interest (I) as the sum of weighted contributions of interest functions evaluated for the different geometric features. The total interest of the j-th pair, which takes values from 0 to 1, is calculated as (Davis et al., 2009):

$$I_j = \frac{\sum_{i=1}^{M} c_i w_i F_{i,j}}{\sum_{i=1}^{M} c_i w_i}, \tag{6}$$

where M is the total number of attributes, c_i is the confident function for the i-th attribute (set here to 1 for the considered ones), $F_{i,j}$ is the i-th attribute interest function evaluated for the j-th pair (see Appendix A), and w_i is the weight assigned to that interest function. In this study, the weight values coincide with the ones proposed by (Duda and Turner, 2021) and are included in Table 4. Apart from simple objects and pairs of objects, MODE also defines clusters as the sets of one or more objects in one field that match a set of one or more objects in the other field (note that here *field* refers to dataset, *i.e.*, observation or forecast).

In this work, the objective of the spatial verification was to complement the point-based verification by considering the reproduction of convective features. Therefore, the temporal verification window was set from 15:30 to 20:00 UTC, corresponding to the intense convective activity. The column-maximum radar reflectivity has been considered as the verification variable. Since reflectivity is not temporally smoothed (in contrast to, *e.g.*, accumulated precipitation), it allows a straightforward comparison of forecast *versus* observed convective structures (Starzec et al., 2018). Notably, the simulated reflectivity is calculated at run time, guaranteeing consistency between its computation and each microphysics parameterization (see (Starzec et al., 2018; Koch et al., 2005)).

Data from three radars of AEMET radar observation system (Sevilla, Malaga and Murcia) were also used to perform a spatial verification of the maximum reflectivity field. Each radar generates a polar volume by scanning 19 PPI at different elevations every 10 min. Since continuous spatial monitoring of the radar echoes along the lifespan of the convective systems was convenient, a composition of the maximum reflectivity field from the three radars was carried out, and a proximity criterion was selected for this purpose.

4. Sensitivity analysis results

This section describes the main verification results. Subsections 4.1 to 4.4 contain point-based verification metrics, whereas Subsection 4.5 is devoted to the spatial verification of column-maximum radar reflectivity. The point-based verification scores are depicted in scatter plots representing IBC using different colors and markers for each microphysics scheme. Apart from a separate plot for each score (BIAS, RSME and ρ), we have also included the corresponding Taylor diagram for each analyzed variable. The numerical values are included in Table B.5.

4.1. Temperature at 2 m

Fig. 13 shows the verification scores for the temperature at 2 m above ground (T_2). All simulations but HG and HT have a cold (negative) BIAS, implying underestimation. In general, all the predictions are good in terms of BIAS with absolute values smaller than 1.6 °C, but some differences exist. Regarding IBC, the best results for T_2 are obtained by configurations based on HRES-IFS, with a maximum absolute value slightly over 0.4 °C, followed by ERA5 with maximum absolute value <0.8 °C. Results obtained with GDAS/FNL and GFS have equivalent values in terms of BIAS with results in between −0.8 °C and − 1.5 °C. Within every IBC, both Goddard and Thompson microphysics exhibit the best performances, with HG being the closest to zero BIAS.

RMSE and ρ results are more similar among simulations. For the former, all tests have a RMSE larger than 2 °C, with H and E performing better than F and G on average. The simulation with HRES-IFS and WDM6 has the lowest RMSE (2.102 °C). No significant differences are found in IBC with respect to ρ, which ranges from 0.784 (ET) to 0.859

Table 4
Attributes weights for total interest computations.

Attribute	Weight
Centroid distance	26.32%
Boundary distance	21.05%
Area ratio	21.05%
Intersection area ratio	10.53%
Complexity ratio	2.63%
Intensity 95th percentile ratio	18.42%

(HD), although simulations with WDM6 and WSM6 are within the uppermost in all cases. Finally, the Taylor diagram shows a better consistency of simulations based on GDAS/FNL and GFS in reproducing the standard deviation of the observed data.

4.2. Relative humidity at 2 m

Verification metrics for the relative humidity at 2 m above ground (RH_2) are depicted in Fig. 15. In this case, five simulations show a dry (negative) BIAS, and fifteen have a humid (positive) one. They range from −1.508% (HD) to 2.865% (GW) and GD is the simulation having the lowest BIAS in absolute value. Within each IBC, microphysics schemes show a similar trend ordered as W-M-T-G-D from highest to lowest BIAS (with sign). Again, RMSE and ρ exhibit smaller differences among simulations, with almost no appreciable differences in ρ. RMSE varies from 12.365% (HM) to 13.749% (FT), while ρ from 0.724 (HG) to 0.779 (GT). Even though the distinction between the different cases is not as substantial as for T_2, we observed that simulations based on ERA5 and HRES-IFS are closer to σ_O than GDAS/FNL and GFS, as can be observed in the Taylor diagram.

4.3. Wind speed at 10 m

Considering the 10 min mean wind speed at 10 m above ground (U_{10}), there is not a remarkable distinction among IBC (Fig. 16). Conversely, microphysics seems to have a more significant influence on the results. Configurations with Morrison microphysics perform best for all IBC and verification metrics, while those with WDM6 have the highest errors. All tests show positive BIAS, being 1.196 m/s the minimum value (HM) and 1.905 m/s the maximum (GD). RMSE oscillates from 2.342 m/s (HM) to 3.126 m/s (ED), and ρ ranges from 0.441 (ED) to 0.584 (FM). Morrison based simulations also have lower CRMSE and σ_F closer to σ_O in the Taylor diagram.

4.4. Accumulated precipitation in 3 h

The accumulated precipitation in 3 h (PCP_{3h}) is the last variable verified by point scores (displayed in Fig. 17). PCP_{3h} shows positive BIAS for five configurations and negative one for the others. This metric ranges from −0.459 mm (FD) to 0.726 mm (EW), being FM the least biased configuration with nearly zero.

Regarding RMSE, ERA5 tests show the highest errors on average, with 4.811 mm being the maximum for EW. However, there is no significant trend among simulations related to IBC or microphysics. The minimum RMSE is shown by FT (3.066 mm). A remarkable aspect of precipitation verification is the spread of the correlation coefficient, which is large compared to other variables. ρ ranges from 0.074 (HW) to 0.639 (ET), and the three uppermost cases are nested to ERA5 (ET, EG and EW). This spread is also appreciable in the Taylor diagram. FT is the case with the least CRMSE, while ED is the configuration closest to σ_O. As commented above in Subsection 3.4 and due to the strongly asymmetric and non smooth nature of precipitation in convection episodes, it is recommendable to complement this verification with spatial methods.

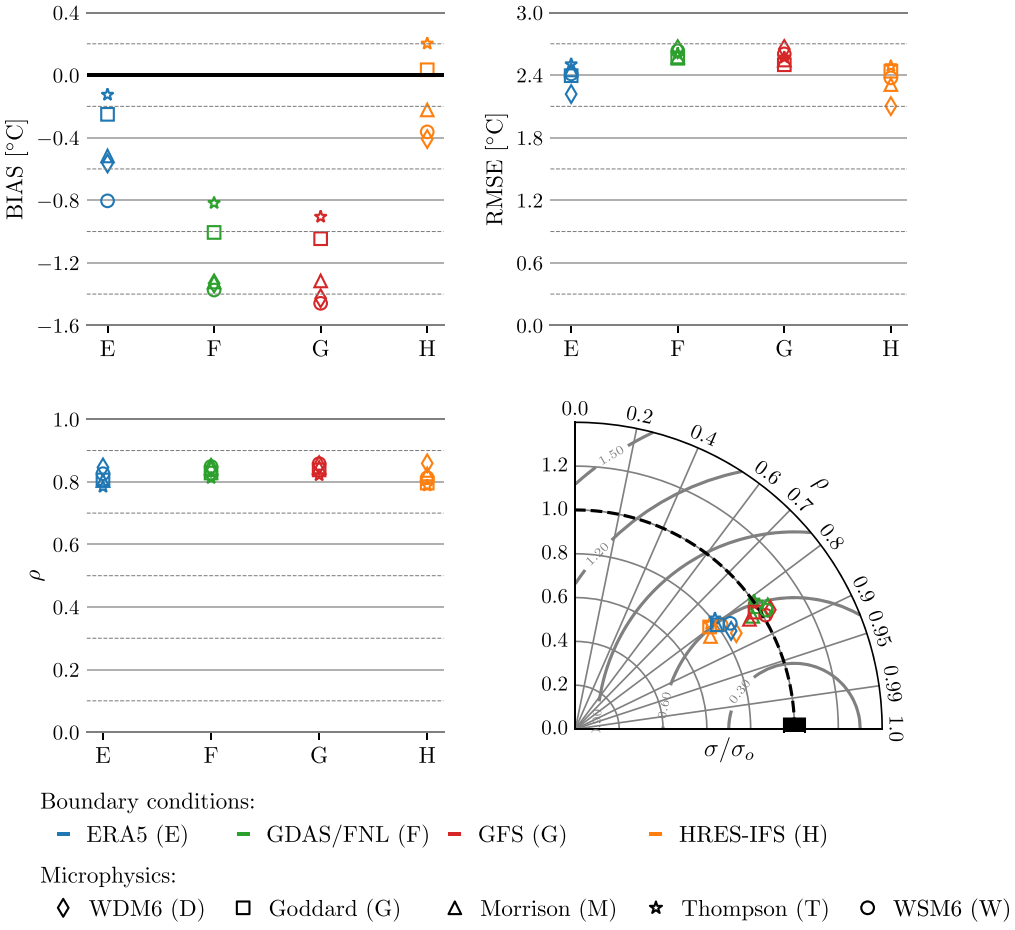

Fig. 14. Verification scores for T_2: BIAS (upper left), Root Mean Square Error (upper right), correlation coefficient (lower left) and Taylor diagram (lower right). The filled black rectangle represents the observation series.

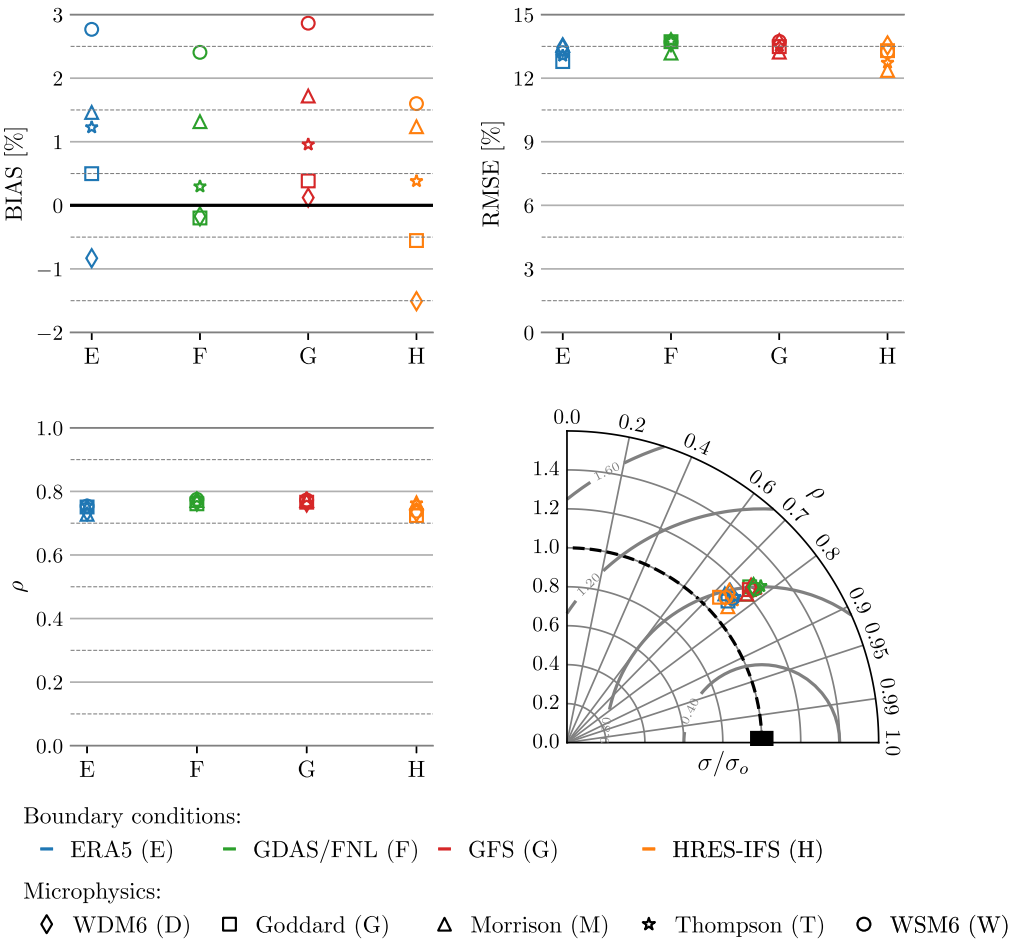

Fig. 15. Verification scores for RH_2: BIAS (upper left), Root Mean Square Error (upper right), correlation coefficient (lower left) and Taylor diagram (lower right). The filled black rectangle represents the observation series.

4.5. Maximum reflectivity

As introduced in Subsection 3.4, spatial verification techniques quantify the effectiveness in reproducing the horizontal structure of precipitation. In this work, we used MODE to evaluate the maximum radar reflectivity simulated by the tested configurations against radar observations during the most intense convection period, from 15:30 to 20:00 UTC.

We have selected an instant of the column-maximum reflectivity field as a sample to qualitatively show the similarities and differences between the radar observation and the simulations. Fig. 18 depicts the column-maximum reflectivity observed by AEMET radars corresponding to 17:30 UTC, when convection is fully developed in the area of interest of this study. According to the echoes intensities, several precipitation regions can be distinguished. At the westernmost part of the map, over Portugal, some disorganized convective cells experience their dissipation stage. This region was active from 15:00 UTC with moderate intensities. Likewise, a stratiform precipitation region in the northernmost zone is associated with the dissipation of disorganized convection. Intense convection cells are observed in the central region, from the north of the province of Malaga to the northern part of Cordoba, and in the northeast of Jaen. They correspond to the most intense and persistent activity, encompassing the whole verification period. Finally, weak echoes and intermittent shallow convection are observed at the southeast over the sea. Several cells reach the provinces of Almeria and Granada towards 18:30 UTC (not shown). Although this precipitation area is not relevant from an observational standpoint, our numerical experiments reproduce significant differences in this region, as detailed below.

Fig. 19 displays simulated column-maximum reflectivity at 17:30 UTC for each pair of IBC and microphysics. From a qualitative point of view, the role of microphysics on the spatial structure of convection seems dominant over IBC (this is also valid for other instants of time, but they are not shown for the sake of brevity). Some schemes, such as Morrison (M) or Thompson (T), are more prone to initiate and spread out convection in larger zones of the center, west, northeast and southeast of the represented area (although the last region is not present for all IBC). Conversely, convection zones based on WDM6 (D), Goddard (G) and WSM6 (W) are less extensive (in that order) and more realistic. For the same IBC, D generally shows the most reduced and the least intense reflectivity cores, whereas (single moment schemes) G and W tend to simulate short-lived isolated cells at the first part of the verification period. The organized convection developing on the border of the provinces of Seville and Malaga is best reproduced by Goddard based simulations, especially with ERA-5 and HRES-IFS IBC.

There also exist similarities among IBC coming from the same dynamical core, *i.e.* ERA5 (E) and HRES-IFS (H) against GDAS/FNL (F) and GFS (G) (see Fig. 19). Precipitation is more intense in the southeast for F and G simulations than E and H, over the Alboran Sea and the province of Almeria. E and H simulations, instead, tend to enhance convection in the northeastern region, which is more consistent with observations. Regardless of the configuration, all the simulations locate

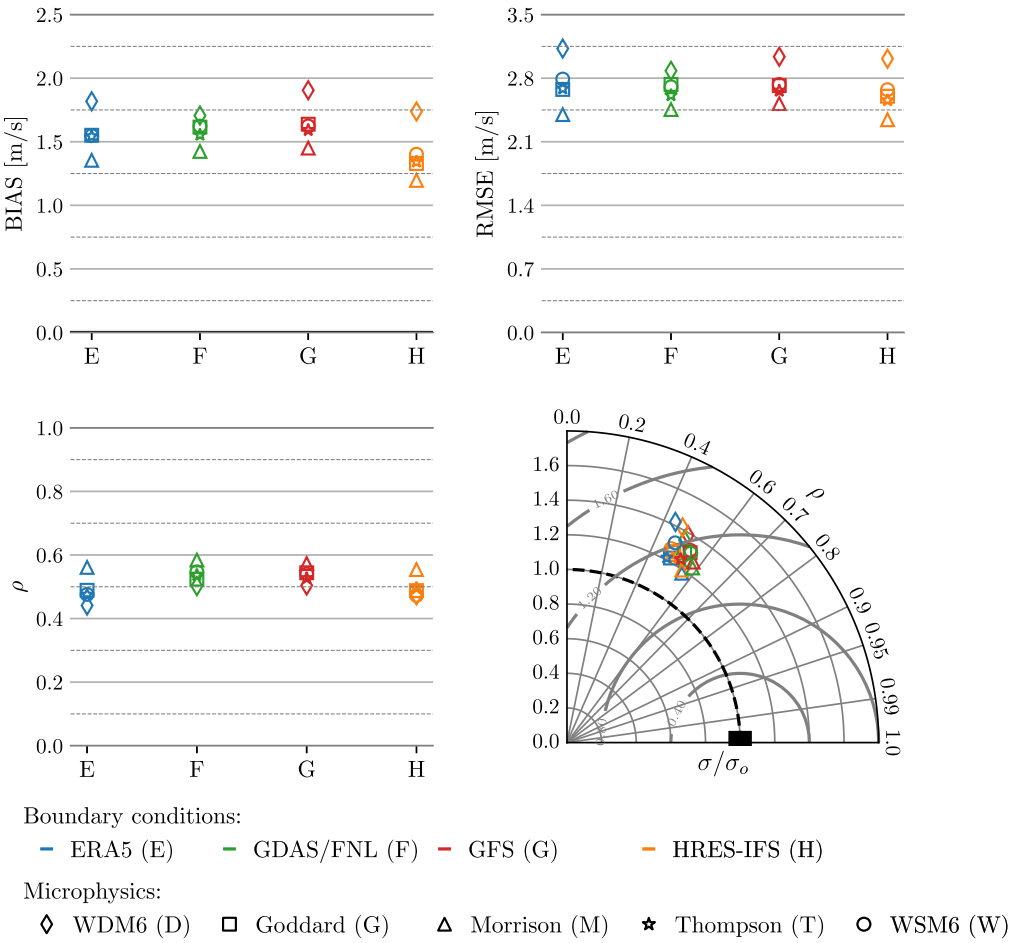

Fig. 16. Verification scores for U_{10}: BIAS (upper left), Root Mean Square Error (upper right), correlation coefficient (lower left) and Taylor diagram (lower right). The filled black rectangle represents the observation series.

a precipitation area in the center of the map, over the province of Cordoba, varying its extent and intensity. Tests based on ERA5 and HRES-IFS reproduce the southern part of this precipitation zone closer to the province of Malaga, as was observed. Also, the anomalous propagation of right-moving cells is evident in some cases, such as ED, EG, EW, HD or HG.

Any raw data, such as the one presented in Figs. 18 and 19, is preprocessed by convolution and thresholding prior to performing the statistical analysis. Fig. 20 illustrates this preprocess through the observed data and two simulated cases, EG and EM, that contain remarkably different spatial structures. Northernmost and western precipitation areas are swept out due to their lesser intensities, and the rest are reduced to their most intense (convective) regions. A total of 14 objects are identified in the observation, while this number is different for the forecasts: 30 in EG and 42 in EM.

After this preprocess for each test and instant, pairs of forecast-observed objects were obtained to evaluate their total interest distributions and, therefore, the quality of predictions. No significant differences were obtained in probability density functions of object pairs (not shown) but they arose when clusters of objects were considered (Fig. 21). The huge variety among the tested configurations is affected by both microphysics and IBC. Considering the quartiles of distributions, ERA5 (E) and HRES-IFS (H) simulations perform the best for Goddard (G). Similarly, GDAS/FNL (F) shows the best results for Thompson (T) and WSM6 (W) and GFS (G) does for WSM6 (W). The configuration consisting of ERA5 and Goddard (EG) shows the highest third quartile (Q3) and second quartile (Q2), and one of the highest values for the first quartile (Q1). Consequently, we did not find any quality improvement enhancing the microphysics scheme complexity, which is coherent with the results reported by (Cassola et al., 2015) for precipitation estimation. According to the interquartile range (IQR), the role of microphysics in the spread of the distributions is more evident than the role of the IBC. IQR ranges from 0.043 for FM to 0.2 for ED. Morrison based configurations (M) show the lowest values of IQR, while WDM6 (D) and Goddard (G) have the highest ones. Finally, there is a general trend to negative skewness (evaluated by means of Yule-Kendall coefficient, Y, which is based on quartiles): 15 distributions have negative Y and 5 have positive Y (4 of which belong to HRES-IFS tests). This index is, in absolute value, lesser than 0.1 for 8 cases of nearly symmetric distributions, being the GDAS/FNL (F) based simulations the most symmetric ones.

In addition to total interest values, the number of forecast objects (n_f) compared with observed objects (n_o) may complement the quality analysis, even though this coefficient is not determinant by itself. The ratio n_f/n_o is represented in Fig. 22, exposing that microphysics is key to this parameter. WDM6 (D) tests have n_f closer to n_o for all IBC, followed by Goddard (G), WSM6 (W), Thompson (T) and Morrison (M). Only HRES-IFS (H) simulations slightly break this trend, which otherwise is coherent with the proneness of each scheme to initiate convective cells observed in raw data (Fig. 19). The simulation consisting of ERA5 and WDM6 (ED) shows the best performance in the number of identified objects, although its total interest values are lower than the outstanding

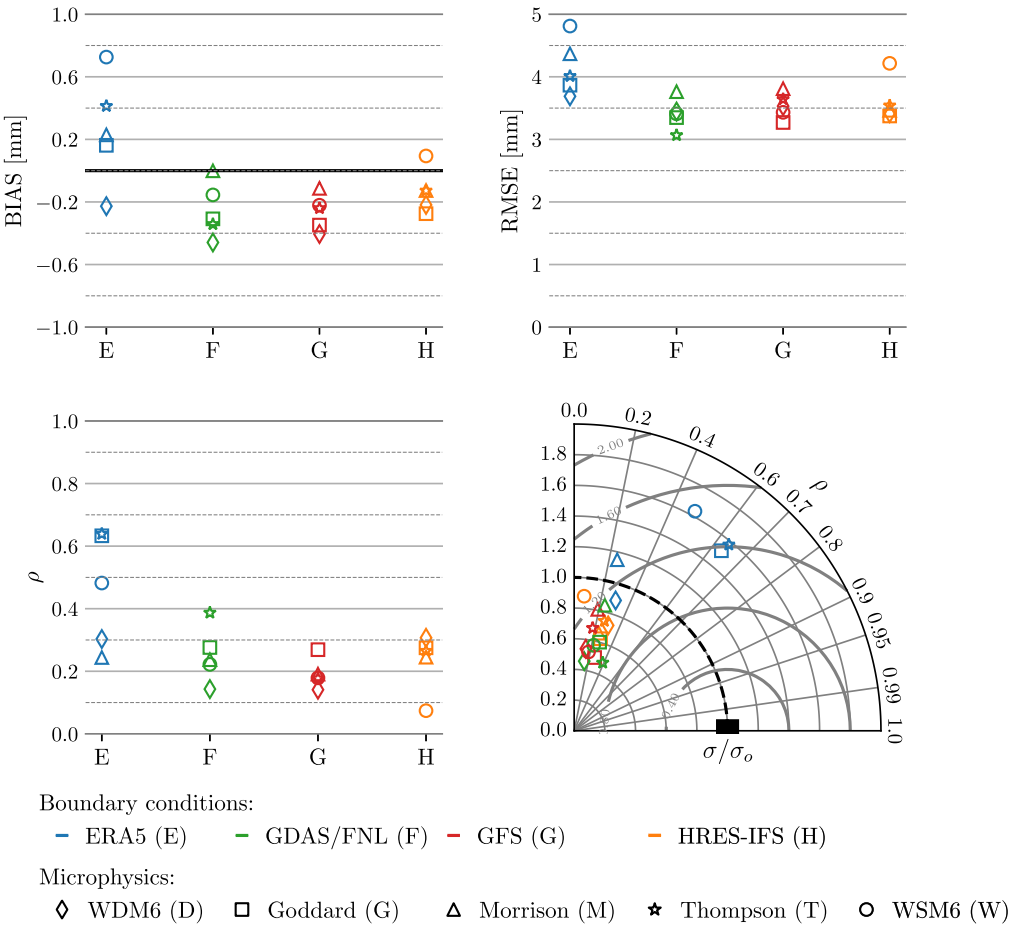

Fig. 17. Verification scores for PCP_{3h}: BIAS (upper left), Root Mean Square Error (upper right), correlation coefficient (lower left) and Taylor diagram (lower right). The filled black rectangle represents the observation series.

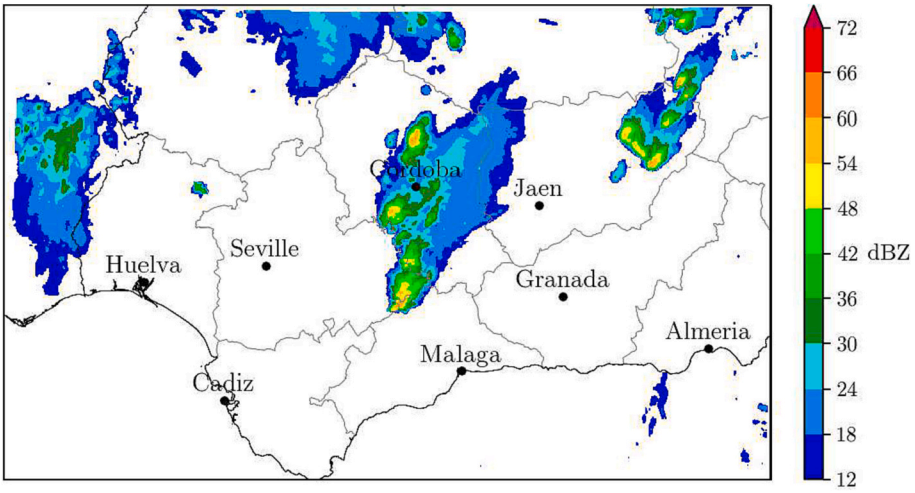

Fig. 18. Observed column-maximum reflectivity at 17:30 UTC.

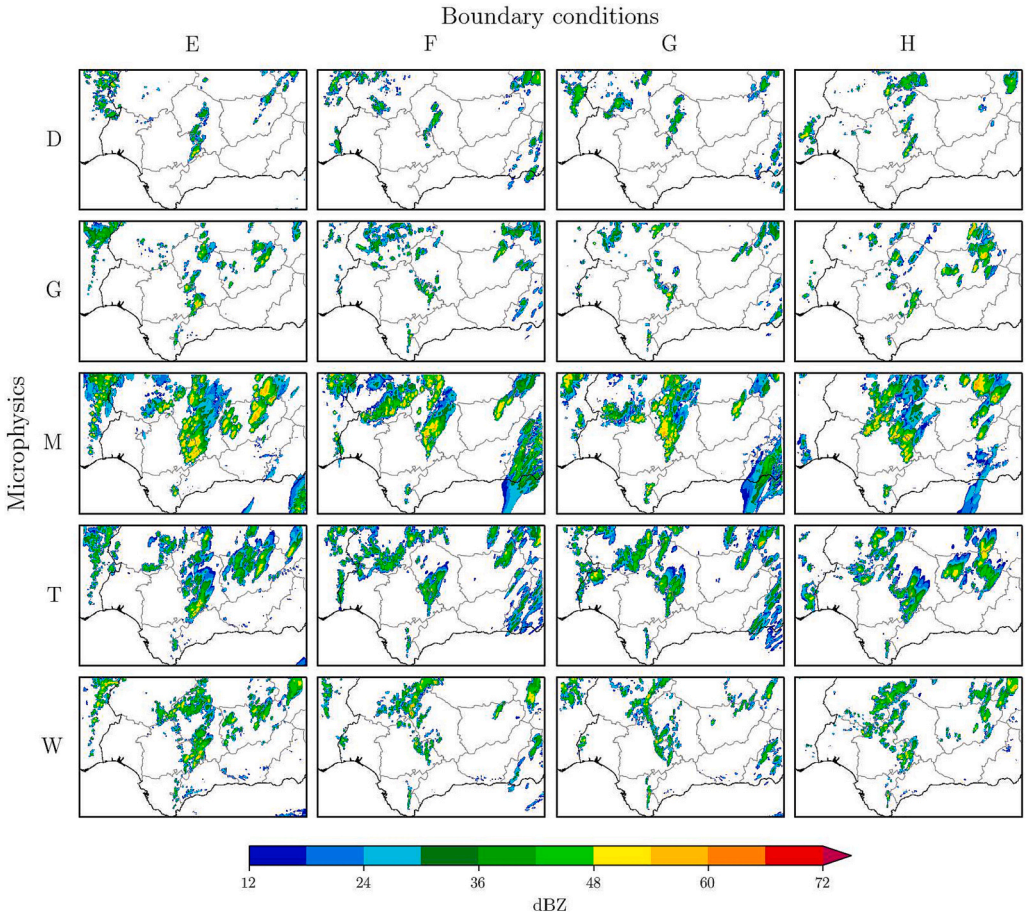

Fig. 19. Simulated column-maximum reflectivity at 17:30 UTC by the different configurations. Initial and boundary conditions are arranged by columns, while microphysics schemes correspond to rows. See Table 3 for abbreviations.

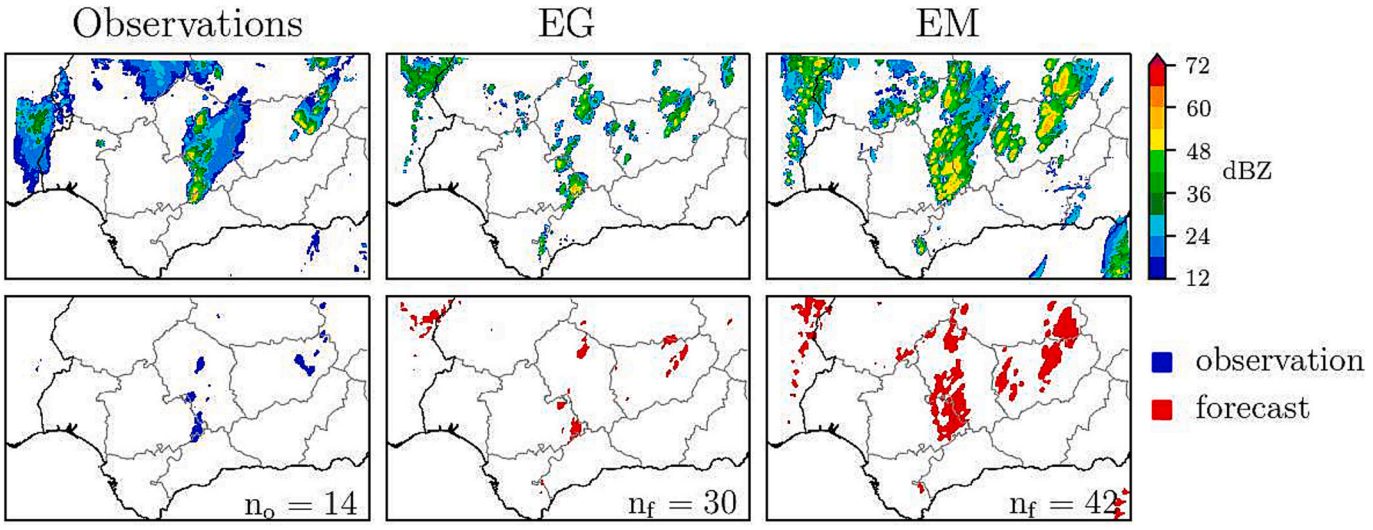

Fig. 20. Applied convolution and thresholding in MODE. First row: raw data of maximum reflectivity. Second row: preprocessed fields. Columns from left to right: observed field for 17:30 UTC, EG predictions, EM predictions (abbreviations in Table 3). n is the number of (observed or forecast) identified objects.

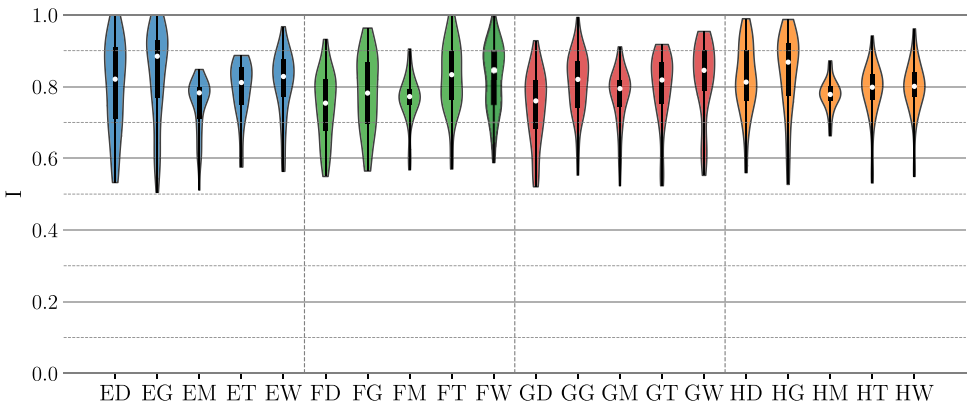

Fig. 21. Total interest probability density functions (pdf) for clusters pairs of observed-forecast objects. Horizontal axis correspond to numerical experiments (abbreviations in Table 3) and shading colors stand for initial and boundary conditions (same as Figs. 13 to 16). Inside each pdf, a box and whisker plot represents the median (white dot), the interquartile range (thick black line) and the whole range of data (thin black line). Vertical grey dashed lines group the experiments by initial and boundary conditions.

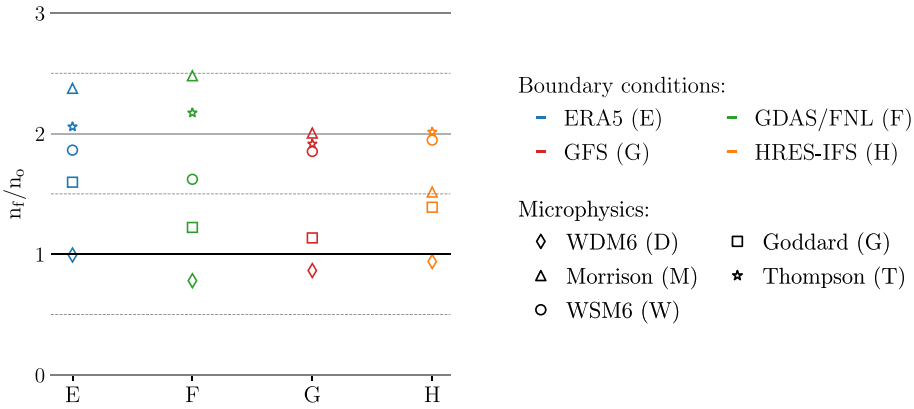

Fig. 22. Number of identified forecast (n_f) and observed (n_o) objects. Vertical axis stands for the n_f/n_o ratio and simulations are arranged by initial and boundary conditions (colors) and microphysics schemes (markers) as Figs. 14 to 17.

EG or HG (see Fig. 21).

4.6. Best overall model

Based on the preceding verification study, we selected the simulation with ERA5 and Goddard microphysics (EG) as the best overall simulation. First of all, focusing on the point-based verification, EG is one of the simulations with smaller BIAS in T_2 and RH_2 having RMSE and ρ comparable results with other simulations. Considering PCP_{3h}, EG is also one of the best simulations even though this parameter is not as representative due to the convective nature of this episode and to the spatial resolution of the simulations. EG is not the best model to predict U_{10} since Morrison has better performance but the differences are not so critical. Second, with a qualitative analysis, EG and HG are the two cases that better simulate the organized convection in the study region, near the border of Malaga and Seville provinces. Lastly, qualitatively considering the pdf of interest of object of clusters, EG shows the highest Q3 and Q2 and one of the best Q1.

Considering all these metrics we have selected the simulation with ERA5 and Goddard microphysics (EG) to analyze the predictability of the tornadic supercell that developed in the north of Malaga that is described in Section 5.

5. Mesoscale analysis for the EG simulation

This section examines convection and organization parameters according to the classic ingredients-based approach (instability, moisture and triggering mechanism (Doswell III et al., 1996)), as well as the simulated supercell structure in EG simulation. Fig. 23 contains maps of some instability indices at three instants within the period of most intense convection (from 15:30 to 20:00 UTC). The interest area exhibits moderate to high values of MUCAPE (exceeding 1000 J/kg up to 2000 J/kg) and low to moderate CIN (below 10 and within 10–50 J/kg) during the whole period. These values are consistent with potential supercell and tornado development environments, provided that deep layer shear is intense (Doswell III and Evans, 2003; Taszarek and Kolendowicz, 2013; Púčik et al., 2015). Furthermore, the lifted condensation level remains under 2000 m AGL and drops to nearly 500 m during the last convection period, when the tornadoes occurred. In addition to the unstable stratification, low-level humidity is also high in the study area, with specific humidity at 850 hPa constantly exceeding 10–12 g/kg (Fig. 24). The low-level convergence zone, where two air masses are encountered, enhances the moisture available for deep moist convection.

Regarding the triggering mechanism, different synoptic and mesoscale processes could jointly start convection in the interest area. Specially relevant are: potential vorticity advection associated with the high levels cut-off low (Fig. 2), low-level convergence between

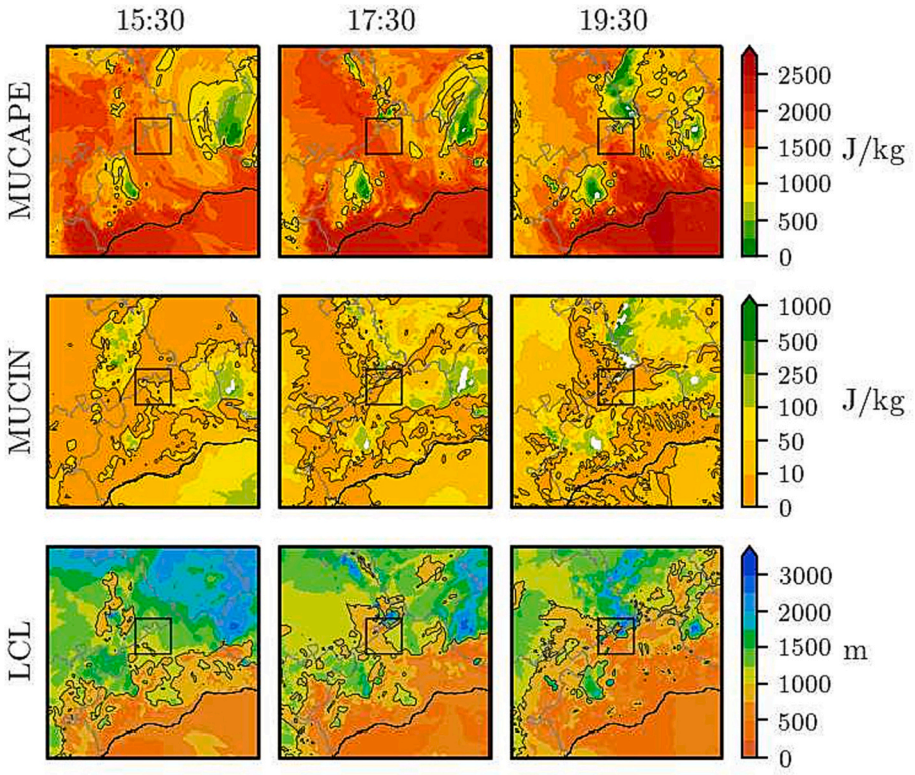

Fig. 23. Instability parameters for EG simulation. Most unstable CAPE (MUCAPE, first row), associated most unstable CIN (MUCIN, second row) and lifted condensation level (LCL, third row). Each column of maps represents one temporal instant within the most convective period of the episode in UTC. Black rectangles highlight the interest area (see Fig. 1). Thin black contour lines emphasize reference levels (MUCAPE = 1000 J/kg, MUCIN = 10 J/kg, LCL = 1000 m).

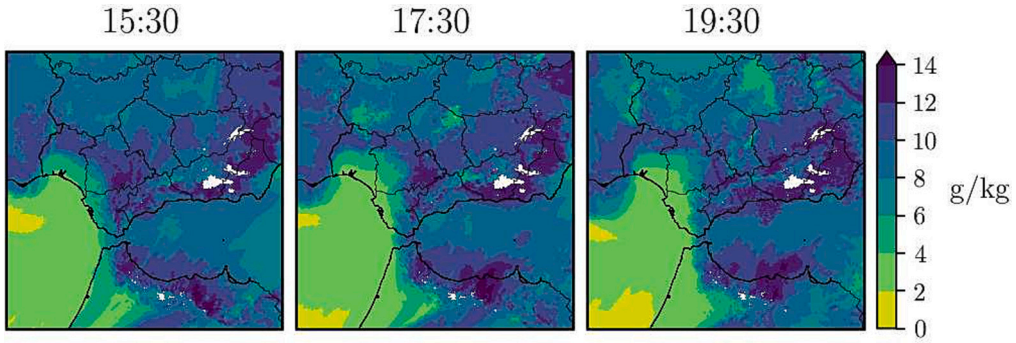

Fig. 24. Specific humidity at 850 hPa for EG simulation. Each column represents one temporal instant within the most convective period of the episode in UTC.

mediterranean southeasterlies and atlantic southwesterlies (Fig. 4), and orographic lifting from the Betic Systems. Apart from these conditions, a favourable environment for supercell development needs sources of organization and rotation, which can be analyzed from Fig. 25. A typical threshold of 20 m/s for deep layer (0–6 km AGL) shear is considered for characterizing this organization environment (Doswell III and Evans, 2003). As seen in the first row of maps, the 0–6 km shear is enough to support supercells development due to the low outlet jet stream impinging over the south of Spain (Figs. 2 and 3). In the interest area, the intensity of 0–6 km shear descends towards the end of the convective episode but still remains over critical values as shown in Fig. 25.

The availability of rotation may be evaluated by means of storm relative helicity (SRH, see Fig. 25 second and third rows). In the interest area, 0–3 km SRH barely reaches 100 m^2/s^2 at the beginning of the convection, when less organized structures developed. However, SRH increases with time to 300–500 m^2/s^2 from 17:30 UTC, when supercellular signatures appeared, see Fig. 26. Analogous behaviour is observed for 0–1 km SRH, associated with potential tornado development (Taszarek and Kolendowicz, 2013). Storm relative helicity in this layer increases with time to almost 500 m^2/s^2 towards the second half of the episode when the tornadoes were observed. Therefore, the EG simulation is consistent with a favourable environment for the observed convective modes.

According to the simulated reflectivity, updraft helicity (UH, see (Cintineo and Stensrud, 2013)), vertical velocity (w) and wind at 700 hPa fields, some supercellular features are reproduced by EG simulation with certain temporal shifts with respect to observations. From 16:30 to

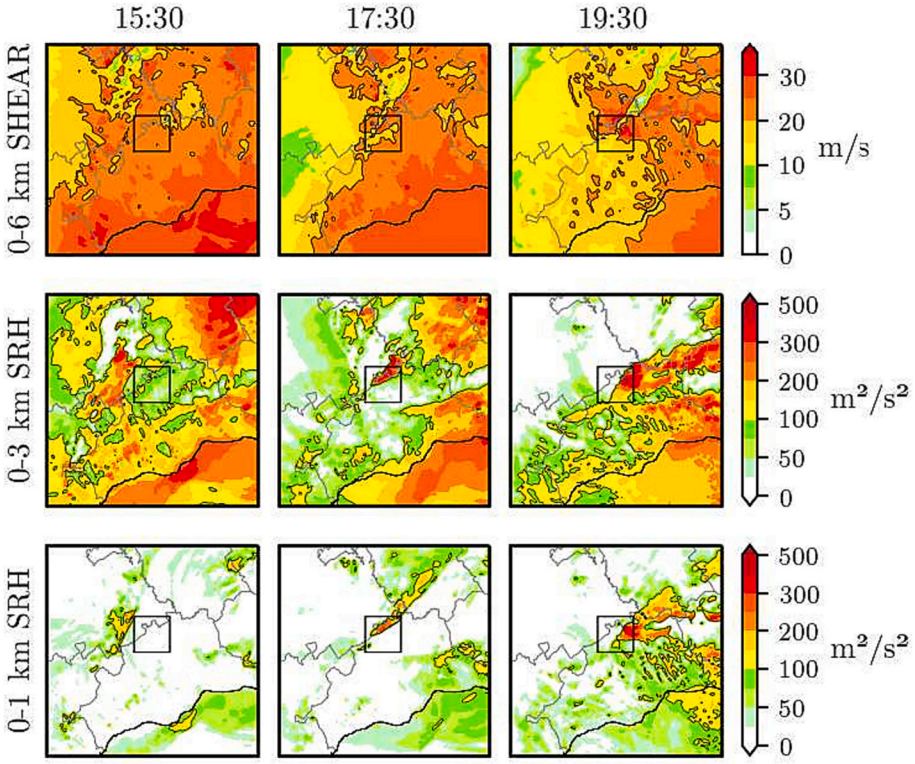

Fig. 25. Kinetic parameters for EG simulation. Deep layer (0–6 km) shear (first row), 0–3 km storm relative helicity (second row) and 0–1 storm relative helicity (third row). Each column of maps represents one temporal instant within the most convective period of the episode in UTC. Black rectangles highlight the interest area (see Fig. 1). Thin black contour lines emphasize reference levels ($SHEAR_{06} = 20\,m/s$, $SRH_{03} = 100\,m^2/s^2$, $SRH_{01} = 100\,m^2/s^2$).

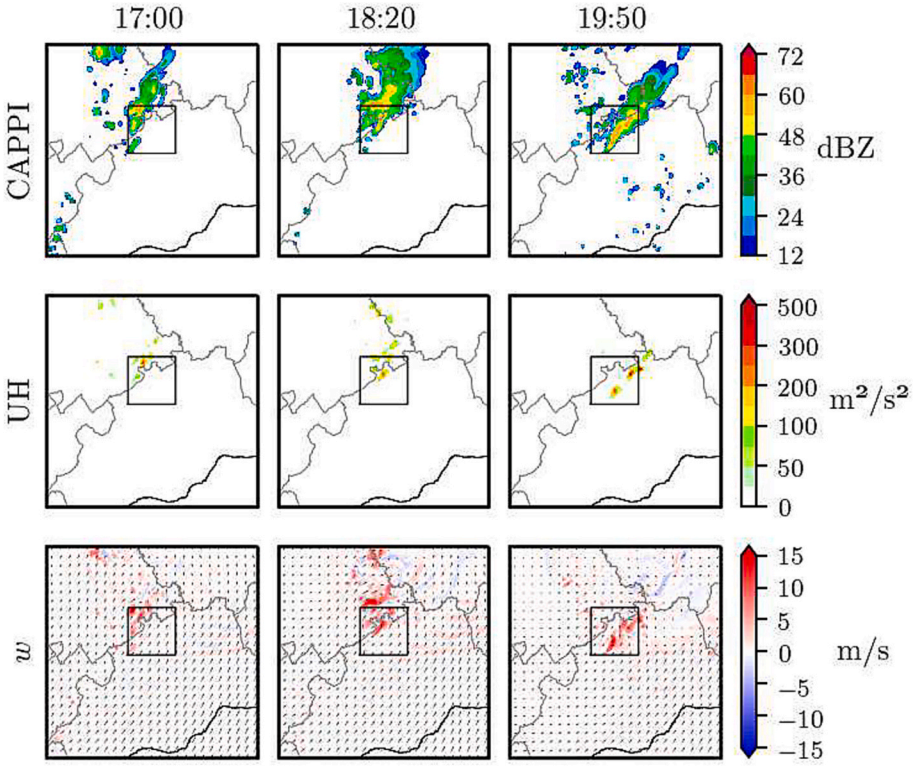

Fig. 26. Supercellular features in EG simulation. CAPPI of simulated radar reflectivity at 2.5 km (first row), updraft helicity (UH, second row), vertical velocity (w) and horizontal wind arrows at 700 hPa (third row). Each column of maps corresponds to one representative instant (in UTC) for the different evolution periods. Black rectangles highlight the interest area (see Fig. 1).

18:00 UTC, some convective cells with 50–60 dBZ in CAPPI at 2.5 km appear. They move northeastward, following the average wind, and some short-lived disperse rotating updrafts are observed. From 18:00 UTC to 19:00 UTC, rotating updrafts are still intermittent, but a strong and persistent reflectivity signal is present with an anomalous southward propagation (to the right of the mean wind). From 19:00 to 20:30 UTC, a rotating updraft becomes persistent accompanying the reflectivity signal and afterwards dissipates. Maps in Fig. 26 depict these different evolution intervals. In comparison with observations (see Subsection 2.2), simulated reflectivity is generally lower than the observed, which has also been reported by other authors (see (Lompar et al., 2017) or (Pilguj et al., 2019)). Moreover, simulated storm trajectory and evolution are delayed about 1 h with respect to observations, similarly to the case described in (Pilguj et al., 2019).

6. Conclusions

This study uses mesoscale simulations to analyze an organized deep moist convection episode on 26 August 2019 in the surroundings of Campillos (Malaga, southern Spain). This event produced a multiple tornado spawning supercell causing several impacts and damages (see Jiménez et al. (Jiménez Alonso et al., 2020) for a vast data collection of this event). The Spanish and European meteorological communities have increasingly studied this type of event in recent years. In Spain, efforts have been devoted to generating supercell databases and characterizing their formation environment. Nevertheless, in contrast to other European countries, there is a lack of mesoscale modelling studies specifically focused on the dynamics and predictability of particular events, and this study aims to fill that gap.

Precisely, we evaluated the performance of WRF model with emphasis on the influence of both microphysics parameterizations and IBC. Simulations accuracy was measured with a combination of traditional point-based scores and spatial verification techniques, which enables consideration of the spatial structure of convection in addition to the verification of surface weather variables. Our results highlight that microphysics schemes represent the key role in simulating this event, with a more significant influence on the results than IBC. Additionally, we have found no significant differences in performance associated with the schemes complexities. Indeed, Goddard parameterization, which is single moment, is the best performing one for ERA5 and HRES-IFS initial and boundary conditions. Morrison, the most complex within the tested schemes, showed the best results in wind verification but was unrealistically prone to initiate and spread out convective cells. Conversely, WDM6 was the most conservative parameterization in convection initiation. Additionally, WDM6 number of simulated objects closely matched the observations, but their quality was lower than in other cases.

The predictions obtained from the combination of ERA5 IBC and Goddard mycrophysics has provided the best performance in the spatial verification results. Even though the predicted reflectivity values are slightly underestimated and the storm evolution is delayed one hour with respect to the observations, this simulation provided instability, shear and helicity conditions coherent with supercells and tornadoes. Furthermore, this configuration allows the explicit simulation of some supercell features as anomalous propagation, the presence of a persistent rotating updraft or simulated reflectivity around 50–60 dBZ.

In conclusion, WRF is capable of reproducing a favourable environment for supercells and tornadoes development for this event, as in other study cases. In spite of exhibiting a temporal shift, the explicit simulation of storms is undoubtedly valuable for severe weather operational forecasting and for supporting decision making. However, sensitivity analyses are still required to enhance our capability of accurately modelling severe weather phenomena. Specifically for this case study, further research is needed to analyze other model components, such as boundary layer parameterizations. In addition, it should be emphasized that the spatial resolution was not sufficiently high to explicitly resolve the formation of tornadoes. Subkilometric simulations could shed light on this issue.

In a global warming context, the thunderstorm frequency will probably intensify. Presumably, severe weather events such as tornadic supercells will be more common, causing increasing damages and fatalities. The processes governing these phenomena are complicated due to their small spatiotemporal scales and high complexity, which hampers correct predictions concerning the development, location and intensity of convective events. Therefore, improving early warning systems through accurate forecasts will become crucial.

CRediT authorship contribution statement

Francisco Javier Bello-Millán: Conceptualization, Data curation, Formal analysis, Investigation, Methodology, Resources, Software, Validation, Visualization, Writing – original draft, Writing – review & editing. **Julián Palacios:** Conceptualization, Data curation, Formal analysis, Investigation, Methodology, Resources, Software, Visualization, Writing – original draft, Writing – review & editing. **Paloma Gutierrez-Castillo:** Conceptualization, Methodology, Supervision, Writing – original draft, Writing – review & editing. **Luis Parras:** Conceptualization, Methodology, Supervision, Writing – original draft, Writing – review & editing.

Declaration of competing interest

The authors declare that they have no known competing financial interests or personal relationships that could have appeared to influence the work reported in this paper.

Data availability

The authors do not have permission to share data.

Acknowledgments

The present simulations were run in AEMET HPC Cirrus. The authors acknowledge Ángel Álvarez for his assistance in the compilation and execution processes. We also thank Carlos Jiménez, C. Manuel Jiménez, Carlos Perea and Jesús Riesco for the valuable information provided. Finally, we thank all the AEMET staff devoted to maintaining and controlling the observational network.

Appendix A. Interest maps

In the spatial verification, the computation of total interest was based on Eq. (6). We considered the following object attributes: centroid distance, boundary distance, area ratio, intersection area ratio, complexity ratio and intensity 95th percentile ratio. Table 4 contains these features along with their respective weights. For each attribute, the corresponding interest function relates any particular value to an interest value for the weighted average calculation of Eq. (6). In this work, the interest functions are piecewise-defined similarly to (Davis et al., 2009), but a correction on distances was made in order to penalize small scale deviations (see Fig. A.27).

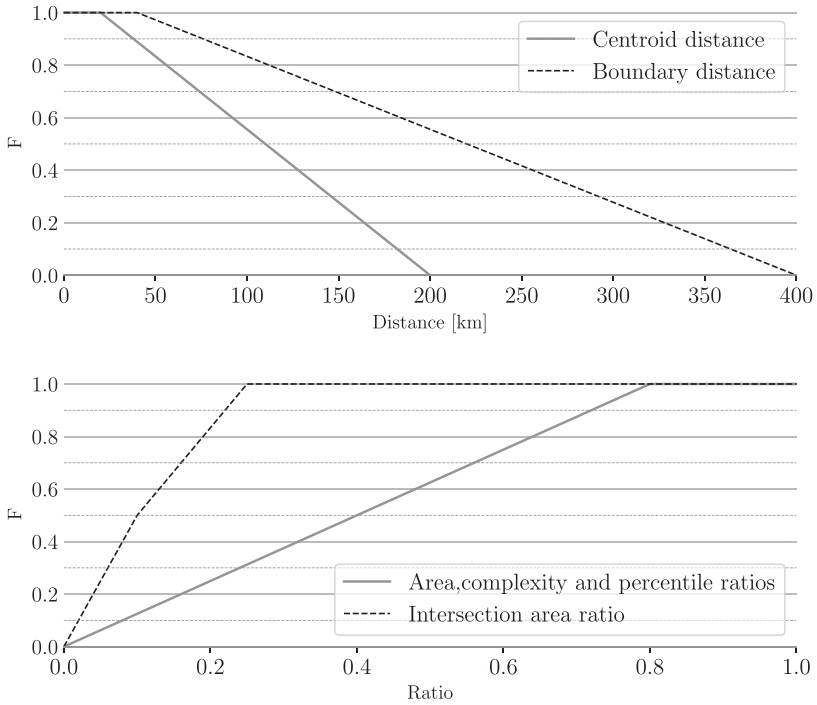

Fig. A.27. Interest functions for centroid distance (solid grey in upper graphic); boundary distance (dashed black in upper graphic); area, complexity and 95th percentile ratios (solid grey in lower graphic); and intersection area ratio (dashed black in lower graphic).

Appendix B. Point-based verification scores

Table B.5 contains all the numerical values which were obtained for the verification parameters to complement the graphical information depicted in Figs. 14 to 17. Each row corresponds to a different numerical experiment, and columns refer to the scores (BIAS, RMSE, and ρ) associated with the point-based verification variables (T_2, RH_2, U_{10} and PCP_{3h}).

Table B.5
Point-based verification scores. Each row corresponds to a numerical test while columns contains the obtained metrics for T_2, RH_2, U_{10} and PCP_{3h}.

Test	$BIAS_{T_2}$ [°C]	$RMSE_{T_2}$ [°C]	ρ_{T_2}	$BIAS_{RH_2}$ [%]	$RMSE_{RH_2}$ [%]	ρ_{RH_2}	$BIAS_{U_{10}}$ [m/s]	$RMSE_{U_{10}}$ [m/s]	$\rho_{U_{10}}$	$BIAS_{PCP_{3h}}$ [mm]	$RMSE_{PCP_{3h}}$ [mm]	$\rho_{PCP_{3h}}$
ED	−0.565	2.218	0.846	−0.832	13.458	0.737	1.818	3.126	0.441	−0.227	3.688	0.303
EG	−0.251	2.394	0.806	0.498	12.784	0.751	1.551	2.676	0.489	0.162	3.866	0.633
EM	−0.517	2.449	0.804	1.461	13.546	0.728	1.354	2.399	0.561	0.229	4.368	0.244
ET	−0.126	2.503	0.784	1.226	13.058	0.756	1.543	2.686	0.475	0.413	4.011	0.639
EW	−0.804	2.411	0.826	2.768	13.205	0.754	1.548	2.790	0.476	0.726	4.811	0.482
FD	−1.332	2.649	0.845	−0.173	13.698	0.768	1.706	2.881	0.502	−0.459	3.445	0.143
FG	−1.006	2.561	0.828	−0.199	13.722	0.761	1.615	2.731	0.524	−0.308	3.348	0.276
FM	−1.323	2.573	0.844	1.316	13.183	0.771	1.424	2.455	0.584	−0.001	3.762	0.237
FT	−0.818	2.605	0.812	0.296	13.749	0.778	1.555	2.612	0.537	−0.342	3.066	0.387
FW	−1.374	2.633	0.849	2.406	13.709	0.775	1.623	2.705	0.547	−0.155	3.408	0.222
GD	−1.427	2.650	0.853	0.121	13.651	0.765	1.905	3.036	0.504	−0.405	3.531	0.141
GG	−1.046	2.499	0.838	0.384	13.488	0.766	1.638	2.718	0.544	−0.348	3.270	0.269
GM	−1.316	2.544	0.846	1.719	13.229	0.771	1.450	2.520	0.573	−0.113	3.810	0.191
GT	−0.906	2.568	0.821	0.956	13.525	0.779	1.592	2.661	0.527	−0.240	3.642	0.177
GW	−1.459	2.603	0.858	2.865	13.736	0.773	1.624	2.731	0.540	−0.221	3.432	0.179
HD	−0.409	2.102	0.859	−1.508	13.546	0.735	1.738	3.014	0.473	−0.219	3.419	0.307
HG	0.034	2.437	0.796	−0.554	13.298	0.724	1.329	2.601	0.488	−0.275	3.374	0.275
HM	−0.223	2.309	0.825	1.236	12.365	0.764	1.196	2.342	0.554	−0.127	3.464	0.245
HT	0.201	2.485	0.788	0.380	12.724	0.762	1.343	2.556	0.496	−0.128	3.540	0.265
HW	−0.363	2.373	0.813	1.600	13.249	0.738	1.402	2.673	0.473	0.094	4.215	0.074

References

Aran, M., Amaro, J., Arús, J., Bech, J., Figuerola, F., Gayà, M., Vilaclara, E., 2009. Synoptic and mesoscale diagnosis of a tornado event in Castellcir, Catalonia, on 18th October 2006. Atmos. Res. 93 (1), 147–160. https://doi.org/10.1016/j.atmosres.2008.09.031.

Bech, J., Pascual, R., Rigo, T., Pineda, N., López, J.M., Arús, J., Gayà, M., 2007. An observational study of the 7 September 2005 Barcelona tornado outbreak. Nat. Hazards Earth Syst. Sci. 7 (1), 129–139. https://doi.org/10.5194/nhess-7-129-2007.

Avolio, E., Miglietta, M.M., 2021. Multiple tornadoes in the Italian Ionian regions: observations, sensitivity tests and mesoscale analysis of convective storm environmental parameters. Atmos. Res. 263 https://doi.org/10.1016/j.atmosres.2021.105800.

Bech, J., Arús, J., Castán, S., Pineda, N., Rigo, T., Montanyà, J., van der Velde, O., 2015. A study of the 21 March 2012 Tornadic quasi linear convective system in Catalonia. Atmos. Res. 158-159, 192–209 doi:j.atmosres.2014.08.009.

Callado Pallarés, A., Escribá, P., Gil Oliva, D., Compte, M., Martnez Sánchez, M., González Herrero, S., Quintero Plaza, D., García-Moya, J.A., 2019. AEMET-gSREPS en operaciones. In: Agencia Estatal de Meteorologa (Ed.), Sexto Simposio Nacional de Predicción, Memorial Antonio Mestre, Madrid, Spain, pp. 351–370. https://doi.org/10.31978/639-19-010-0.351 (in Spanish).

Calvo-Sancho, C., Díaz-Fernández, J., Martín, Y., Bolgiani, P., Sastre, M., González-Alemán, J.J., Santos-Muñoz, D., Farrán, J.I., Martín, M.L., 2022. Supercell convective environments in Spain based on ERA5: hail and non-hail differences. Weather Clim. Dynam. 3 (3), 1021–1036. https://doi.org/10.5194/wcd-3-1021-2022.

Cassola, F., Ferrari, F., Mazzino, A., 2015. Numerical simulations of Mediterranean heavy precipitation events with the WRF model: a verification exercise using different approaches. Atmos. Res. 164, 210–225. https://doi.org/10.1016/j.atmosres.2015.05.010.

Cintineo, R.M., Stensrud, D.J., 2013. On the predictability of supercell thunderstorm evolution. J. Atmos. Sci. 70 (7), 1993–2011. https://doi.org/10.1175/jas-d-12-0166.1.

Consorcio de Compensación de Seguros, 2021. Estadística riesgos extraordinarios. Serie 1971–2021, Tech. rep., Ministerio de Asuntos Económicos y Transformación Digital., Madrid (in Spanish).

Davis, C., Brown, B., Bullock, R., 2006. Object-based verification of precipitation forecasts. Part I: Methodology and application to mesoscale rain areas. Mon. Weather Rev. 134 (7), 1772–1784. https://doi.org/10.1175/mwr3145.1.

Davis, C.A., Brown, B.G., Bullock, R., Halley-Gotway, J., 2009. The method for object-based diagnostic evaluation (MODE) applied to numerical forecasts from the 2005 NSSL/SPC Spring Program. Weather Forecast. 24 (5), 1252–1267. https://doi.org/10.1175/2009waf2222241.1.

Delle Monache, L., Nipen, T., Liu, Y., Roux, G., Stull, R., 2011. Kalman filter and analog schemes to postprocess numerical weather predictions. Mon. Weather Rev. 139 (11), 3554–3570. https://doi.org/10.1175/2011mwr3653.1.

Doswell III, C.A., Evans, J.S., 2003. Proximity sounding analysis for derechos and supercells: an assessment of similarities and differences. Atmos. Res. 67, 117–133. https://doi.org/10.1016/S0169-8095(03)00047-4.

Doswell III, C.A., Brooks, H.E., Maddox, R.A., 1996. Flash flood forecasting: an ingredients-based methodology. Weather Forecast. 11 (4), 560–581. https://doi.org/10.1175/1520-0434(1996)011<0560:FFFAIB>2.0.CO;2.

Duda, J.D., Turner, D.D., 2021. Large-sample application of radar reflectivity object-based verification to evaluate HRRR Warm-season forecasts. Weather Forecast. 36 (3), 805–821. https://doi.org/10.1175/waf-d-20-0203.1.

ECMWF, 2019. IFS Documentation CY46R1. ECMWF. https://doi.org/10.21957/juw9gfhn2.

Farr, T.G., Rosen, P.A., Caro, E., Crippen, R., Duren, R., Hensley, S., Kobrick, M., Paller, M., Rodriguez, E., Roth, L., et al., 2007. The shuttle radar topography mission. Rev. Geophys. 45 (2) https://doi.org/10.1029/2005RG000183.

Gayà, M., 2011. Tornadoes and severe storms in Spain. Atmos. Res. 100 (4), 334–343. https://doi.org/10.1016/j.atmosres.2010.10.019.

Gayà, M., Homar, V., Romero, R., Ramis, C., 2001. Tornadoes and waterspouts in the Balearic Islands: phenomena and environment characterization. Atmos. Res. 56 (1), 253–267. https://doi.org/10.1016/S0169-8095(00)00076-4.

Gilleland, E., Ahijevych, D., Brown, B.G., Casati, B., Ebert, E.E., 2009. Intercomparison of spatial forecast verification methods. Weather Forecast. 24 (5), 1416–1430. https://doi.org/10.1175/2009waf2222269.1.

Hersbach, H., Bell, B., Berrisford, P., Hirahara, S., Horányi, A., Muñoz-Sabater, J., Nicolas, J., Peubey, C., Radu, R., Schepers, D., Simmons, A., Soci, C., Abdalla, S., Abellan, X., Balsamo, G., Bechtold, P., Biavati, G., Bidlot, J., Bonavita, M., Chiara, G. D., Dahlgren, P., Dee, D., Diamantakis, M., Dragani, R., Flemming, J., Forbes, R., Fuentes, M., Geer, A., Haimberger, L., Healy, S., Hogan, R.J., Hólm, E., Janisková, M., Keeley, S., Laloyaux, P., Lopez, P., Lupu, C., Radnoti, G., de Rosnay, P., Rozum, I., Vamborg, F., Villaume, S., Thépaut, J.N., 2020. The ERA5 global reanalysis. Q. J. R. Meteorol. Soc. 146 (730), 1999–2049. https://doi.org/10.1002/qj.3803.

Hong, S.-Y., Lim, J.-O.J., 2006. The WRF single-moment 6-class microphysics scheme (WSM6). Asia-Pac. J. Atmos. Sci. 42 (2), 129–151.

Hong, S.-Y., Noh, Y., Dudhia, J., 2006. A new vertical diffusion package with an explicit treatment of entrainment processes. Mon. Weather Rev. 134 (9), 2318–2341. https://doi.org/10.1175/mwr3199.1.

Iacono, M.J., Delamere, J.S., Mlawer, E.J., Shephard, M.W., Clough, S.A., Collins, W.D., 2008. Radiative forcing by long-lived greenhouse gases: calculations with the AER radiative transfer models. J. Geophys. Res.-Atmos. 113 (13) https://doi.org/10.1029/2008jd009944.

Jolliffe, I.T., Stephenson, D.B., 2012. Forecast Verification: A practitioner's Guide in Atmospheric Science. John Wiley & Sons.

Karki, R., Hasson, S. Ul, Gerlitz, L., Talchabhadel, R., Schenk, E., Schickhoff, U., Scholten, T., Böhner, J., 2018. WRF-based simulation of an extreme precipitation event over the Central Himalayas: Atmospheric mechanisms and their representation by microphysics parameterization schemes. Atmos. Res. 214, 21–35. https://doi.org/10.1016/j.atmosres.2018.07.016.

Klemp, J.B., Rotunno, R., 1983. A study of the Tornadic region within a supercell thunderstorm. J. Atmos. Sci. 40 (2), 359–377. https://doi.org/10.1175/1520-0469(1983)040<0359:ASOTTR>2.0.CO;2.

Koch, S.E., Ferrier, B., Stoelinga, M.T., Szoke, E., Weiss, S.J., Kain, J.S., 2005. The use of simulated radar reflectivity fields in the diagnosis of mesoscale phenomena from high-resolution WRF model forecasts. In: Preprints, 11th Conf. on Mesoscale Processes, 7. Amer. Meteor. Soc., J4J, Albuquerque, NM, pp. 1–9.

Kumar, P., Kishtawal, C., Pal, P., 2017. Impact of ECMWF, NCEP, and NCMRWF global model analysis on the WRF model forecast over Indian Region. Theor. Appl. Climatol. 127, 143–151. https://doi.org/10.1007/s00704-015-1629-1.

Lim, K.-S.S., Hong, S.-Y., 2010. Development of an effective double-moment cloud microphysics scheme with prognostic cloud condensation nuclei (CCN) for weather and climate models. Mon. Weather Rev. 138 (5), 1587–1612. https://doi.org/10.1175/2009MWR2968.1.

Liu, Y., Chen, X., Li, Q., Yang, J., Li, L., Wang, T., 2020. Impact of different microphysics and cumulus parameterizations in WRF for heavy rainfall simulations in the central segment of the Tianshan Mountains, China. Atmos. Res. 244, 105052 https://doi.org/10.1016/j.atmosres.2020.105052.

Lompar, M., Ćurić, M., Romanic, D., 2017. Simulation of a severe convective storm using a numerical model with explicitly incorporated aerosols. Atmos. Res. 194, 164–177. https://doi.org/10.1016/j.atmosres.2017.04.037.

Martín, Y., Cívica, M., Pham, E., 2021. Constructing a supercell database in Spain using publicly available two-dimensional radar images and citizen science. Ann. Am. Assoc. Geogr. 111 (5), 1346–1366. https://doi.org/10.1080/24694452.2020.1812371.

Morrison, H., Thompson, G., Tatarskii, V., 2009. Impact of cloud microphysics on the development of trailing stratiform precipitation in a simulated squall line: Comparison of one-and two-moment schemes. Mon. Weather Rev. 137 (3), 991–1007. https://doi.org/10.1175/2008mwr2556.1.

National Centers for Environmental Prediction, National Weather Service, NOAA, U.S. Department of Commerce, 2015a. NCEP GFS 0.25 Degree Global Forecast Grids Historical Archive. https://doi.org/10.5065/d65d8pwk.

National Centers for Environmental Prediction, National Weather Service, NOAA, U.S. Department of Commerce, 2015b. NCEP GDAS/FNL 0.25 Degree Global Tropospheric Analyses and Forecast Grids. https://doi.org/10.5065/d65q4t4z.

Pilguj, N., Taszarek, M., Łukasz Pajurek, M. Kryza, 2019. High-resolution simulation of an isolated tornadic supercell in Poland on 20 June 2016. Atmos. Res. 218, 145–159. https://doi.org/10.1016/j.atmosres.2018.11.017.

Púčik, T., Groenemeijer, P., Rỳva, D., Kolář, M., 2015. Proximity soundings of severe and nonsevere thunderstorms in Central Europe. Mon. Weather Rev. 143 (12), 4805–4821. https://doi.org/10.1175/mwr-D-15-0104.1.

Riemann-Campe, K., Fraedrich, K., Lunkeit, F., 2009. Global climatology of convective available potential energy (CAPE) and convective inhibition (CIN) in ERA-40 reanalysis. Atmos. Res. 93 (1–3), 534–545. https://doi.org/10.1016/j.atmosres.2008.09.037.

Riesco, J., Mora, M., de Pablo, F., Rivas, L., 2014. Regimes of intense precipitation in the Spanish Mediterranean area. Atmos. Res. 137, 66–79. https://doi.org/10.1016/j.atmosres.2013.09.010.

Rodríguez, O., Bech, J., 2018. Sounding-derived parameters associated with tornadic storms in Catalonia. Int. J. Climatol. 38 (5), 2400–2414. https://doi.org/10.1002/joc.5343.

Rodríguez, O., Bech, J., 2021. Tornadic environments in the Iberian Peninsula and the Balearic Islands based on ERA5 reanalysis. Int. J. Climatol. 41 (S1), E1959–E1979. https://doi.org/10.1002/joc.6825.

Rodríguez, O., Lemus-Canovas, M., 2023. Synoptic patterns triggering tornadic storms on the Iberian Peninsula and the Balearic Islands. Atmos. Res., 106634 https://doi.org/10.1016/j.atmosres.2023.106634.

Romero, R., Ramis, C., Homar, V., 2015. On the severe convective storm of 29 October 2013 in the Balearic Islands: observational and numerical study. Q. J. R. Meteorol. Soc. 141 (689), 1208–1222. https://doi.org/10.1002/qj.2429.

Sánchez-Laulhé, J., 2005. El tornado de Cádiz de 1671. Boletín Asociación Meteorológica Española (AME) 9, 11–15 (in Spanish).

Sánchez-Laulhé, J.M., Riesco, J., Polvorinos, F., Soriano, J.D., 2014. Synoptic and mesoscalar environments associated with the heavy local rainfall on 16 August 2010 in the south of the Iberian Peninsula, Tethys. J. Mediterranean Meteorol. Climatol. 11, 11–23. https://doi.org/10.3369/tethys.2014.11.02.

Schwitalla, T., Branch, O., Wulfmeyer, V., 2020. Sensitivity study of the planetary boundary layer and microphysical schemes to the initialization of convection over the Arabian Peninsula. Q. J. R. Meteorol. Soc. 146 (727), 846–869. https://doi.org/10.1002/qj.3711.

Skamarock, W.C., Klemp, J.B., Dudhia, J., Gill, D.O., Liu, Z., Berner, J., Wang, W., Powers, J.G., Duda, M.G., Barker, D.M., et al., 2021. A description of the advanced research WRF model version 4. In: NCAR Technical Note 145 (NCAR/TN-556+STR), p. 145. https://doi.org/10.5065/1dfh-6p97.

Jiménez Alonso, C., Jiménez Cavero, C.M., Perea Hitos, C., Riesco Martín, J., 2020. Estudio meteorológico de la supercélula tornádica del 26 de agosto de 2019 en Campillos (Málaga), Nota Técnica de AEMET, p. 33. https://doi.org/10.31978/666-20-021-7 (in Spanish).

J. A. Quirantes Calvo, F. J. Bello Millán, M. Cívica Corrales, J. Palacios García, 2022. Caracterización del ambiente convectivo en la formación de supercélulas en España en el periodo 2017-2021, Nota Técnica de AEMET 38, (in Spanish). doi:10.31978/666-22-010-9.

Spiridonov, V., Ćurić, M., Velinov, G., Jakimovski, B., 2021. Numerical simulation of a violent supercell tornado over Vienna airport initialized and initiated with a cloud model. Atmos. Res. 261 https://doi.org/10.1016/j.atmosres.2021.105758.

Starzec, M., Mullendore, G.L., Kucera, P.A., 2018. Using radar reflectivity to evaluate the vertical structure of forecast convection. J. Appl. Meteorol. Climatol. 57 (12), 2835–2849. https://doi.org/10.1175/jamc-d-18-0116.1.

Tao, W.-K., Simpson, J., McCumber, M., 1989. An ice-water saturation adjustment. Mon. Weather Rev. 117 (1), 231–235. https://doi.org/10.1175/1520-0493(1989)117<0231:aiwsa>2.0.co;2.

Tao, W.-K., Simpson, J., Baker, D., Braun, S., Chou, M.-D., Ferrier, B., Johnson, D., Khain, A., Lang, S., Lynn, B., Shie, C.-L., Starr, D., Sui, C.-H., Wang, Y., Wetzel, P., 2003. Microphysics, radiation and surface processes in the Goddard Cumulus Ensemble (GCE) model. Meteorog. Atmos. Phys. 82, 97–137. https://doi.org/10.1007/s00703-001-0594-7.

Tapiador, F.J., Marcos, C., Sancho, J.M., 2019. The convective rainfall rate from cloud physical properties algorithm for Meteosat Second-Generation satellites: microphysical basis and intercomparisons using an object-based method. Remote Sens. 11 (5), 527. https://doi.org/10.3390/rs11050527.

Taszarek, M., Kolendowicz, L., 2013. Sounding-derived parameters associated with tornado occurrence in Poland and Universal Tornadic Index. Atmos. Res. 134, 186–197. https://doi.org/10.1016/j.atmosres.2013.07.016.

Taszarek, M., Czernecki, B., Walczakiewicz, S., Mazur, A., Kolendowicz, L., 2016. An isolated tornadic supercell of 14 July 2012 in Poland - a prediction technique within the use of coarse-grid WRF simulation. Atmos. Res. 178-179, 367–379. https://doi.org/10.1016/j.atmosres.2016.04.009.

Taylor, K.E., 2001. Summarizing multiple aspects of model performance in a single diagram. J. Geophys. Res. Atmos. 106 (D7), 7183–7192. https://doi.org/10.1029/2000jd900719.

Tewari, M., Chen, F., Wang, W., Dudhia, J., LeMone, M., Mitchell, K., Ek, M., Gayno, G., Wegiel, J., Cuenca, R.H., 2004. Implementation and verification of the unified Nah land surface model in the WRF model (Formerly Paper Number 17.5). In: A. M. Society (Ed.), Proceedings of the 20th Conference on Weather Analysis and Forecasting/16th Conference on Numerical Weather Prediction, Seattle, WA, USA, 14.

Thompson, G., Field, P.R., Rasmussen, R.M., Hall, W.D., 2008. Explicit forecasts of winter precipitation using an improved bulk microphysics scheme. Part II: Implementation of a new snow parameterization. Mon. Weather Rev. 136 (12), 5095–5115. https://doi.org/10.1175/2008mwr2387.1.

Tiedtke, M., 1989. A comprehensive mass flux scheme for cumulus parameterization in large-scale models. Mon. Weather Rev. 117 (8), 1779–1800. https://doi.org/10.1175/1520-0493(1989)117<1779:acmfsf>2.0.co;2.

W. Thiao, R. A. Scofield, J. Robinson, 1993. The Relationship between water vapor plumes and extreme rainfall events during the summer season, NOAA Technical Report NESDIS 67.

Toker, E., Ezber, Y., Sen, O.L., 2021. Numerical simulation and sensitivity study of a severe hailstorm over Istanbul. Atmos. Res. 250 https://doi.org/10.1016/j.atmosres.2020.105373.

Wilks, D.S., 2019. Statistical Methods in the Atmospheric Sciences, , Fourth edition100. Academic Press. https://doi.org/10.1016/c2017-0-03921-6.